University of Plymouth

PEARL **https://pearl.plymouth.ac.uk**

Faculty of Science and Engineering School of Biological and Marine Sciences

2020-07-15

Bidirectional bedform fields at the head of a submarine canyon (NE Atlantic)

Lo Iacono, C

http://hdl.handle.net/10026.1/15740

10.1016/j.epsl.2020.116321
Earth and Planetary Science Letters
Elsevier BV

All content in PEARL is protected by copyright law. Author manuscripts are made available in accordance with publisher policies. Please cite only the published version using the details provided on the item record or document. In the absence of an open licence (e.g. Creative Commons), permissions for further reuse of content should be sought from the publisher or author.

*Manuscript Rev Lo Iacono et al., 2019
Click here to view linked References

Accepted 1 May 2020

Bidirectional bedform fields at the head of a submarine canyon (NE Atlantic).

Claudio Lo Iacono[1,2]*, Jorge Guillen[1], Queralt Guerrero[1], Ruth Duran[1], Catherine Wardell[2], Rob Hall[3], Tahmeena Aslam[3], Gareth Carter[4], Jenny Gales[5], Veerle A.I. Huvenne[2]

[1] *Marine Sciences Institute, Spanish National Research Council, Paseo Maritimo de la Barceloneta 37-49, 08003 Barcelona, Spain*

[2] *National Oceanography Centre, University of Southampton, Waterfront Campus, Southampton, United Kingdom*

[3] *Centre for Ocean and Atmospheric Sciences, School of Environmental Sciences, University of East Anglia, Norwich Research Park, Norwich, United Kingdom*

[4] *British Geological Survey, The Lyell Centre, Research Avenue South, Edinburgh, United Kingdom*

[5] *University of Plymouth, School of Biological and Marine Sciences, Drake Circus, Plymouth, PL4 8AA, United Kingdom*

*: corresponding author. E-mail address: loiacono@icm.csic.es

ABSTRACT

Submarine canyons are known to force ocean mesoscale circulation and local hydrodynamics. Alternate up- and down-canyon near-bottom flows have been widely documented along the upper reaches, connecting the canyon heads with the contiguous outer shelves and vice versa. Nonetheless, we still miss clear evidence of bedform fields expressing these complex patterns. In this study, through a multi-scale analysis in both space and time, we document rare asymmetric bedforms, up to 880 m long and 10 m high, developing within a depth range of 168-220 m at the head of the Whittard Canyon (NE Atlantic). One field of well-developed sandwaves has an atypical up-slope asymmetry, with the steeper slope facing the shallower regions of the shelf, and

contrasting with surrounding down-slope sandwaves facing the canyon. The bedforms are interpreted to represent both up-slope and down-slope bottom currents connecting the upper reaches of the canyon to the outer shelf on the southern Celtic Margin, in the Bay of Biscay. The sandwaves were surveyed with shipboard Multibeam bathymetry (5 m grid cell resolution), AUV sidescan sonar (0.15 m grid cell resolution) and ROV footage, and sampled with three ROV-mounted vibro-cores and two box-cores. Sidescan sonar mosaics groundtruthed by ROV footage and sediment samples show with unprecedented detail spectacular trains of fresh overprinting megaripples, previously undocumented sand peaks and bowl-shaped depressions on the crests of the tallest sandwaves. Differences in sedimentary settings and benthic habitats indicate that these features are currently active in particularly dynamic areas, allowing for very slow migration of sandwaves. Modelling of the internal tide regime together with concurrent hydrographic observations suggest large-amplitude semi-diurnal internal tides, possibly transitioning to asymmetric internal bores, as the main mechanism maintaining the mapped up-slope sandwaves. This work highlights the importance of uncommon sediment dynamics in canyon head environments and adds insight to the traditional notions of gravity-driven processes, being dominant in these environments, envisaging implications for improving geo-hazard assessment of mobile substrates and quantification of offshore sediment and carbon fluxes.

Keywords: Bedforms, seafloor mapping, marine robotics, geomorphology, submarine canyons, internal tides

1. INTRODUCTION

The increasing detail of high-resolution mapping of bedform fields across several continental shelves around the world is regularly revealing uncommon morphological

patterns related to complex and variable sedimentary and hydrodynamic regimes. For example, observations on coastal and inner shelf settings report sandwave fields migrating in opposite directions related to intricate hydrodynamic patterns (Van Landeghem et al., 2012; Jiang and Lin, 2016). The dynamics of these bedforms are generally controlled by the interplay of storm-forced currents and steered residual tidal flows, acting over a variable local geomorphology (Boe et al., 2009; Van Landeghem et al., 2012).

However, present-day activity of bedforms on sediment-starved outer shelf settings, deeper than 100 m and far from modern fluvial sediment inputs, is still poorly understood, mainly due to the lack of detailed seafloor mapping and long-term hydrodynamic observations. In these settings, which are less sensitive to coastal hydrodynamics and storm-induced flows, sandwave dynamics are mainly related to along-shelf geostrophic circulation, generally reactivating relict sandy deposits developed during previous sea-level stages (Lo Iacono et al, 2010; Rovere et al., 2019).

These hydrodynamic patterns can become more complex in the vicinity of shelf-incising submarine canyons (Allen and Durrieu de Madron, 2009; Li et al., 2019). The upper reaches of canyons are major conduits for down-slope gravitational flows funnelling sediments to the deep-sea (Piper and Normark, 2009; Paull et al., 2011; Azpiroz-Zabala et al., 2017), and may also promote up- and down-slope sediment transport related to amplified internal waves (Allen and Durrieu de Madron, 2009; Puig et al., 2013; Li et al., 2019). However, we are still missing clearly documented evidence of bedform field migration in relation to such hydrodynamic processes, connecting the canyon head to the shallower adjacent shelf and vice versa. Yet, these findings may have relevant implications in ensuring the long-term integrity of offshore infrastructures (e.g. wind-farm foundations, subsea pipelines, and tele-communication cables) close to mobile

81 substrates, in addition to better defining the patterns of organic and oxygen rich fluxes
82 across continental margins (Ahmerkamp et al., 2015). During the JC125 CODEMAP
83 Cruise, aimed to map and quantify complex deep-sea habitats of the Whittard Canyon
84 (NE Atlantic), we used a combination of routine and advanced marine robotic
85 technologies (shipboard / Autonomous Underwater Vehicle (AUV) mapping, Remotely
86 Operated Vehicle (ROV)-mounted vibro-cores, box-cores, ROV footage), to document
87 atypical bedform fields, mapped on the Celtic outer shelf between 168 and 220 m water
88 depth, showing contrasting geomorphological patterns at the head of the eastern canyon
89 branch (Fig. 1). We: 1) describe the morphology and sedimentology of different
90 superimposed bedforms, 2) examine the role of the Whittard Canyon in their generation
91 and evolution, with specific reference to internal tides, and 3) discuss their long- and
92 short-term dynamics.

93 **2. GEOLOGICAL AND OCEANOGRAPHIC SETTING**

94 The Celtic margin is a passive continental margin that extends WNW-ESE between the
95 Goban Spur and the Berthois Spur (Bourillet et al., 2006, Fig. 1). The continental shelf,
96 connected with the English Channel, is up to 500 km wide and connects with a steep
97 structurally controlled continental slope (average 8°). The geomorphology of the shelf is
98 irregular, with around 45 linear sand ridges, 40 to 180 km long, crossing the shelf
99 roughly perpendicular to the continental slope between 100 m and 200 m water depth
100 (Bouysse et al., 1976; Praeg et al., 2015) (Fig. 1a). These ridges correspond to
101 glacigenic sand banks formed between 20 and 12 ka BP (Pantin and Evans, 1984;
102 Scourse et al., 2009) and have been partially reworked by tidal flows during the last
103 marine transgression (Berné et al., 1998; Reynaud et al., 1999). The Whittard Canyon,
104 200 km long, is the largest of several submarine canyons incising the Celtic margin
105 (Mulder et al., 2012; Amaro et al., 2016). It extends from the shelf-edge, 200 m deep, to

the base of the continental slope, 4500 m deep (Bourillet et al., 2006; Mulder et al., 2012; Fig. 1a). Four dendritic V-shaped branches are controlled by persistent headward erosion, which creates sub-vertical walls with exposed Cretaceous to Pleistocene sedimentary successions (Carter et al., 2018 and references therein). The sandwaves presented in this study were previously interpreted as relict features active during the Last Glacial Maxima (Cunningam et al., 2005). Two hundred km SE from the sandwave field presented here, up to 1 km long active sandwaves were described on the La Chapelle Bank, and interpreted as being controlled by barotropic (surface) tidal residual velocities, although baroclinic (internal) tides could play a role in their dynamics in proximity of the shelf-edge (Heathershaw and Codd, 1985).

Tidal currents in the Celtic Sea region are dominated by semi-diurnal (twice daily) constituents and 75% of the kinetic energy can be attributed to the principal lunar semi-diurnal constituent (M_2) (Pingree, 1980). Along the Celtic margin, barotropic tidal currents vary in magnitude over the spring-neap cycle, from 0.2 m s^{-1} during neaps to 0.5 m s^{-1} during spring (Sharples et al., 2007). The semi-major axis of the M_2 tidal ellipse is orientated NE-SW, across the slope (Pingree et al., 1999). This tidal ellipse orientation, along with a density stratified water column, allows the generation of internal waves with tidal frequencies (internal tides).

The highly corrugated slopes of the upper canyon and outer shelf generate a complex internal tide field (Vlasenko et al., 2014) and on-shelf propagating waves are dissipated close to the shelf-edge (Hopkins et al., 2014). Strong tidal currents and breaking internal waves within Whittard Canyon are expected to enhance the turbulent mixing of physical and biogeochemical properties through the water column, especially near the canyon heads, and may also generate near-bed internal bores, which increase sediment

resuspension and along-canyon transport (Amaro et al., 2016; Hall et al., 2017; Aslam et al., 2018).

3. MATERIAL AND METHODS

Most of the dataset used for this study has been collected during the JC125 Cruise, carried out in 2015 aboard the RRS "James Cook", in the frame of the CODEMAP Project ("Complex Deep-sea Environments: Mapping habitat heterogeneity As Proxy for biodiversity" - ERC Starting Grant). The shipboard Multibeam (MB) system was the 100 kHz Kongsberg EM710, producing a Digital Terrain Model (DTM) at a grid cell resolution of 5 m. An additional MB dataset, aimed to extend the mapping of bedforms around the area, was collected with the same MB system in 2018 during the JC166 Cruise, aboard the RRS "James Cook" (part of the NERC funded CLASS programme). Two AUV "Autosub6000" Side Scan Sonar (SSS) missions and one MB survey were performed during JC125. AUV navigation was achieved using a RDI Doppler Velocity Log (DVL) inertial navigation system (dead-reckoning) linked to a GPS fix before descending and a Ultra-Short Baseline (USBL) position at the start of the mission. To minimize the AUV drift during the dives, its position was also recalculated at the end of each mission by USBL if the ship was in the vicinity, or by GPS surface location once emerged.

The AUV-SSS was the 410 kHz EdgeTech FS2200. SSS mosaics were produced at a grid cell resolution of 15 cm using the software PRISM, developed at the National Oceanography Centre (NOC). The AUV-MB system was a 200 kHz Kongsberg EM2040, allowing for the production of a DTM at a grid cell resolution of 2 m. The ROV "ISIS" performed two dives on a western region where AUV-SSS was previously acquired, to groundtruth the area using an integrated vibro-corer. The ROV-vibro-core strongly improved the precision of sampling operations, in parallel with a visual

155 groundtruth of the local habitats. ROV navigation was achieved using a Sonardyne
156 USBL, in parallel with Doppler dead-reckoning calculated through a RDI DVL. Three
157 ROV vibro-cores were collected from different bedform settings (sand peak: VC_129,
158 sandwave stoss: VC_131-1, sandwave trough: VC_131-2) with penetrations of 98 cm,
159 74 cm and 43 cm respectively. The ROV camera was an OKEANOS Insite Mini Zeus
160 HD 1920 x 1080, equipped with two parallel laser pointers 10 cm apart. Two additional
161 box-cores were collected (sandwave stoss: BC_147, sandwave crest: BC_148) and sub-
162 sampled, resulting in core lengths of 19 cm and 20 cm respectively. Samples from
163 sediment cores were collected every 5 centimetres and dried at 80°C for 24 hours. The
164 sediment fraction finer than 2000 μm was examined using an LA-950V2 laser scattering
165 particle size distribution analyser (HORIBA), while the coarser fraction was sieved for
166 6000, 4000 and 2000 μm.
167 1270 bathymetric transects orthogonal to the sandwave crests and spaced 20 m each
168 other were extracted from the bathymetric grids, and morphometric indices (wavelength
169 λ, height h, asymmetry index (AI), migration rates) calculated. The sandwave
170 wavelength (L=L1+L2) is defined as the distance from trough to trough, compensated
171 for slope inclination α (Fig. 2). The sandwave height (h) is calculated as the orthogonal
172 from the highest point of the bedform (crest) to the baseline (Fig. 2). Following the
173 method of Knaapen (2005), the asymmetry index (AI) is defined as the difference of the
174 distances between the crest and the upslope and downslope troughs, divided by the
175 wavelength (L2−L1)/L (Fig. 2). Positive and negative AI values are indicative of
176 downslope and upslope asymmetry respectively. Sandwaves with AI between -0.2 and
177 0.2 were considered as symmetric. Coordinates and elevations were obtained every 20
178 m along each transect. Hull-mounted MB bathymetry (15 m grid cell resolution)
179 acquired in 2000 by the Geological Survey of Ireland in the frame of the INFOMAR

Project was compared to the JC125 MB dataset (5 m grid cell resolution) to assess the migration rate of the mapped sandwaves over a period of 15 years.

4. RESULTS

4.1 Geomorphology of the Whittard bedforms

The sandwave field was mapped across a 25 by 9 km wide sector of the outer shelf, with a 0.1° gradient on average, within a depth range of 164-210 m (Fig.1b). The outer shelf is incised between 200 m and 220 m by the heads of two adjacent tributaries of the eastern branch of the Whittard Canyon, defined here as western and eastern tributaries (Fig.1b). The average wavelength of the sandwaves is 367 m, with a maximum of 880 m (Fig. S1). Their height displays an average value of 4 m, with a maximum of 10.4 m (Fig. S1). All sandwaves are approximately parallel to the shelf-edge, directed perpendicular to the axes of the two tributaries (Fig. 1b).

Asymmetry is significantly different between the regions of mapped sandwaves (Fig. 3). Sandwaves adjacent to the western tributary display up-slope asymmetric trends, with average AI values of -0.3 and minimum of -0.95 (Fig. S1). At an average depth of 190 m, these sandwaves become symmetric for a limited portion of the shelf and become down-slope asymmetric at shallower depths (Fig. 3). In the transition between up-slope and down-slope asymmetry, all three trends can coexist on the same sandwaves, reflecting convergent sediment transport directions (Fig. 3). Down-slope asymmetry becomes dominant towards the easternmost sector of the shelf, where AI values display an average of 0.29, increasing up to 0.9 (Fig. 3, Fig. S1). Two sub-areas (named western and eastern fields hereafter) located 10 km apart in front of the western and eastern tributaries, were mapped at high resolution with the AUV (Figs. 4-7, Fig. S2).

Furthermore, the western field was groundtruthed with ROV visual observations, vibro-cores and box-cores.

Western field - The western field displays a sandwave train between 188 m and 240 m water depth (Fig. 4). Their average wavelength is 387 m, with a maximum value of 671 m, the average height being 5.2 m, with a maximum value of 10.4 m (Fig. S3). The western sandwaves are up-slope asymmetric (average value AI: -0.33, minimum value: -0.94) (Fig. S3), with their asymmetry decreasing towards the shallower sectors, suggesting a net sediment transport directed from the canyon head to the outer shelf (Fig. 3). Crests, approximately parallel and occasionally bifurcated, are mostly NW-SE oriented (120°) and up to 10 km long (Fig. 3). AUV-SSS mapping revealed that 2D megaripples and complex 3D features occur on the entire western field (Figs. 4, 5). Almost all the megaripples display an up-slope asymmetry, coherent with the sandwaves on which they are superimposed (Fig. 8a).

At the head of the western tributary, at a depth between 205 m and 230 m, a dense network of asymmetric megaripple trains occurs with a height of up to 1 m and a variable wavelength ranging between 10 m and 45 m (Figs. 4, 5a). Along this sector, megaripples organize in a herringbone pattern with a bimodal orientation: NW-SE (140°-160°) and WNW-ESE (100°-110°) (Fig. 4). Moreover, megaripples here are occasionally interrupted by longitudinally aligned sand peaks, alternating crests and troughs for up to 110 m long in a NE-SW direction (47°-60°) (Fig. 5a). Towards shallower depths, megaripple wavelength decreases, ranging between 6 m and 14 m, with the longest occurring close to the sandwave crests, and their height being 0.5 m on average (Fig. 5b). Their main orientation is NW-SE (130°-160°), forming a clockwise angle of 10°-40° offset with the sandwave crests (Figs. 4, 5). Megaripples are generally

absent on a low-energy "shadow zone" sheltered by the sandwave crests, in some case displaying low backscatter facies suggesting fine sediment textures (Figs. 5b, c, d). The shadow zone covers the troughs and which becomes progressively larger moving up-slope (Fig. 4). In parallel, moving up-slope, megaripples concentrate exclusively on the sandwave crests, losing their relief and lateral continuity (Figs. 4, 5c, 8a). The tallest sandwaves of the western field display on their crests roughly circular depressions regularly and closely spaced, 10-15 m wide, and up to 0.4 m deep (Fig. 5b). To our knowledge, these intriguing features, defined as bowl-shaped depressions, have never been described in previous works.

Eastern field - Sandwaves of the eastern field occur at a depth between 178 m and 201 m, where they are interrupted at the shelf margin, incised by the head of the eastern tributary canyon (Fig. 1b, Fig. S2). They display an average wavelength of 324 m, with a maximum value of 574 m, and an average height of 3.1 m, with a maximum value of 7.5 m (Fig. S3). The eastern sandwaves are NW-SE oriented (average orientation: 134°), their crests being linear or slightly sinuous. They present a positive asymmetry index (average AI: 0.12, maximum AI: 0.78) (Fig. S3), being directed towards the head of the tributary canyon and contrasting with the opposite trend of the western field (Fig. S2). AUV-SSS and MB data collected on the eastern field display a dense network of superimposed megaripple trains, 5 to 15 m long and up to 0.5 m high (Figs. 6,8b, Fig. S2). These megaripples are observed on the sandwave stoss sides and close to the crests, and are less frequent along the trough (Figs. 7a, 8b). They develop in a similar direction to the sandwaves crests (NW-SE), or offset by a clockwise angle of 20-30° with them (Fig. 6). Their morphology ranges between slightly symmetrical to asymmetrical, with their asymmetry increasing close to the sandwave crests and being consistent with the

sandwaves migrating towards the canyon (Fig. 8b). This is also reflected by the high backscatter facies on some of the crests, suggesting coarse sediments controlled by high-energetic hydrodynamics, changing to low backscatter on the following downslope lee, coinciding with fine-sediment in sheltered low-energy environments (Figs. 7b, 7b1). The crests of the most pronounced sandwaves in the eastern field display in most cases an uncommon two-fold morphology in plan view, consisting of two, or three, megaripple crests running parallel to the sandwave crest (Figs. 6, 7b). The two-fold crests can laterally pass to 3D geomorphologies, defined here as tear-drop shaped lobes, 0.4-0.8 m deep, stretching for 30 to 40 m along the direction of the sandwave crests (Figs. 6, 7b).

Finally, a dense network of asymmetric megaripples directed towards deeper depths has been mapped on the canyon head (Figs. 7c, d). These megaripples are 5 to 20 m long and 0.5 to 0.8 m high. In limited areas of this region, megaripples merge their crests to form 3D sub-circular features, 20-40 m wide and 0.5-1 m deep (Figs. 7c, d).

4.2 Groundtruthing data

Sediment cores

Vibro-cores (VC) and box-cores (BC) reveal a dominant sandy grain size, although their spatial variability reflects different morpho-sedimentary environments within the sampled bedforms. The core collected on a sand peak of the western field (VC_129, Fig. 9a), consists of well sorted yellow medium sands throughout the entire 98 cm long core, except for an increase to coarse and very coarse sands between 20 and 30 cm below the surface (Fig. 9). The core does not present any stratification or internal structure. Two cores were collected on the stoss side (VC_131-1) and in the trough (VC_131-2) of the same sandwave (Fig. 9b). On the sandwave stoss side, where superimposed megaripples are evident on the SSS mosaic (Fig. 9b), VC_131-1 consists

of greenish muddy layers for the first 3 cm, coarsening to well sorted brownish medium sands until the depth of 38 cm (Fig 9). Below this level, sediment grain size changes to moderately sorted medium sands with armouring gravelly layers consisting of scattered broken shells, 1 to 2 cm large, down to the base of the core, at 74 cm (Fig. 9). In the trough of the same sandwave, VC_131-2 shows bioturbated sediments with a finer sediment texture, consisting of greenish poorly sorted muddy sands, becoming stiff from 35 cm to the base of the core, 43 cm deep (Fig. 9). Coarse broken shells occur between 12 and 15 cm and a layer of well laminated bioclasts (mainly Scaphopoda) is evident between 28 and 31 cm, sustained by a matrix of medium and fine sands (Fig. 9). Two box-cores were collected in the same region (Fig. 9). BC_147, located on the sandwave crest, is dominated by well sorted and winnowed yellow medium sands, without any internal structure across its length (21 cm). BC_148, 18 cm deep, is located in the trough of the sandwave, nearby VC_131-2 (Fig. 9), and consists of strongly bioturbated poorly sorted greenish silty fine sands. Several burrows inhabited by worms were observed on the top and within the first 10 cm of this box-core (Fig. 9).

Seabed video observations

The ROV videos collected during the vibro-core operations show different aspects of the seafloor in the sampled regions. The sampled sand peak is fully covered by superimposed sharp-crested up-canyon asymmetric ripples and almost a total absence of benthic fauna has been observed, except for a few sparse holothurians (Fig. 10a). Relevant changes were observed in the ROV transect moving from VC_131-1 to VC_131-2. The stoss region (location of VC_131-1) was characterized by faded up-slope ripples and by the presence of mainly mobile fauna (starfish, crabs, holothurians, fishes) (Fig. 10b). Getting close to the sandwave crest, fresh ripples were observed

superimposed on the megaripples, displaying the same orientation and asymmetric trends (Figs. 10c, d). Similarly to the location of VC_129, very few organisms were observed on the ROV video when approaching the crest (Figs. 10c, d). Down-slope of the sandwave crest, ripples tended to fade out in the trough, coinciding with the region of the SSS mosaic in which megaripples cease to occur. In parallel, bioturbation increased, and several sessile organisms, mainly anemones, were observed at the VC_131-2 sampling location (Fig. 10e).

5. DISCUSSION

5.1 Up-slope and down-slope outer-shelf bedforms around the Whittard Canyon

The application of advanced marine robotic technologies unveiled spectacular fields of bedforms at the head of the Whittard Canyon. Up- and down-slope asymmetric bedforms, spanning centimetre to kilometre scales, reflect the occurrence of peculiar sediment dynamic processes which connect the outer shelf domain with the heads of submarine canyons and vice versa. The bedforms are mainly composed of sandy sediments, which most likely consist of coastal bioclastic deposits produced during previous sea-level lowstands (Scourse et al., 2009) and reworked since the last sea-level transgressive stage until the present day. The distribution, orientation and asymmetry observed on the bedforms surrounding the head of the western tributary suggest that these sandwaves are related to strong up-canyon near-bottom currents which rise up the canyon rim onto the surrounding outer shelf (Fig. 11).

We rule out the interpretation of these bedforms as up-slope migrating cyclic steps, as these features are generally controlled by channelized density currents on steep slopes, alternating super and sub-critical flows (Parker, 1996; Paull et al., 2011; Slootman and Cartigny, 2020). None of the above mentioned environmental conditions are observed

329 in the study area. The up-canyon migrating 3D megaripples and the alligned sand peaks
330 mapped at the head of this canyon (Figs. 4, 5a) probably reflect the most energetic
331 hydrodynamic regime of the entire study area, requiring up to 1 m s^{-1} fast currents to
332 form (Southard and Boguchwal, 1990). Both the directions of megaripples (NW-SE and
333 WNW-ESE) and of aligned sand peaks (NE-SW) are consistent with along-canyon-axis
334 near-bottom currents, orientated NE-SW.
335 Moreover, the ongoing action of strong up-slope flows is confirmed by the large
336 "shadow areas" on the stoss sides of the sandwaves, often coinciding with low
337 backscatter facies, and by the megaripples superimposed on the sandwaves (SSS
338 observation) (Figs. 5b, c, d), which in turn host fresh ripples (ROV visual observations)
339 (Figs. 10c, d), all of them displaying similar asymmetric trends and particularly
340 complex patterns around the sandwave crests (Figs. 4, 5b,d). The divergence angle of
341 20°-35° between megaripple and sandwave crests is probably due to the deflection of
342 local flows induced by the variable geomorphology (Van Dijk and Kleinhans, 2005).
343 Moving away from the canyon head, the intensity of up-slope bottom currents
344 progressively dissipates, with the megaripples fading on the sandwave stoss sides and
345 tending to develop exclusively on their crests (Fig. 4).
346 Up-slope bedform asymmetry ceases at around 190 m water depth, coinciding with the
347 upper limit of sandwave bifurcations, indicating that the canyon-sourced sediment
348 transport direction is limited to the region surrounding the canyon head (Figs. 3, 11).
349 Shallower and to the side of the canyon head, the sandwaves become symmetric and
350 transition to down-slope asymmetric (Figs. 3, 11). The orientation of down-slope
351 sandwaves coincides with the direction of the regional across-shelf tidal currents, which
352 have a dominant NE-SW direction (Amaro et al., 2016). On the deepest sector of the
353 shelf, at an average depth of 190 m, down-slope sandwaves are interrupted by the head

of the eastern tributary canyon, which incises the outer shelf deposits (Figs. 3, 6, 11). The superimposed megaripples of the eastern field are equally down-slope asymmetric, controlled by bottom currents directed towards the canyon head (Figs. 6, 7a, b), where intense down-slope gravity currents can generate rounded 3D megaripples (Figs. 6c,d, 11). These bedform fields suggest that the Whittard Canyon is an active conduit for sediment transport processes funnelling coarse sediments down to the deep sea.

5.2 The role of Whittard Canyon in the generation and maintenance of up-slope sandwaves

To our knowledge, this work presents the first extensive seafloor expression of up-slope bottom currents rising over the rim of a submarine canyon onto the outer shelf. Some older works based on low-resolution geophysical datasets have described sandwave dynamics hinting at similar hydrodynamic forcing along the upper reaches of other canyons (Knebel and Folger, 1976; Karl et al., 1986). Seismic records revealed the occurrence of up-slope asymmetric sandwaves at the head of Navariski Canyon (Bering Sea) (Karl et al., 1986) and at the outer shelf adjacent to the head of Wilmington Canyon (US Atlantic margin) (Knebel and Folger, 1976). The sandwaves, perpendicular to the canyon axis, are composed of fine sands and resemble the dimensions of the sandwaves described here. The suggested mechanisms responsible for sandwave migration were in both cases internal waves with a tidal or shorter period, which once channelized along the canyon axis would increase in strength and transport sediments towards the canyon head (Knebel and Folger, 1976; Karl et al., 1986).

Barotropic tides over abrupt and sloping canyon morphologies can locally generate internal tides (Hotchkiss and Wunsch, 1982; Hall and Carter 2011), and form up-slope propagating internal tidal bores during critical or near-critical reflection (Dauxois and

Young, 1999; Legg and Adcroft, 2003). These conditions are met when the geometric slope of internal tides (determined by wave frequency, stratification strength, and latitude) is approximately equal to the canyon-axis morphological slope. During near-critical reflection, internal wave energy is trapped near the sloping boundary and typically results in non-linear effects, wave breaking, and, if the forcing internal tide is strong enough, the formation of an internal bore (Hall et al., 2017). Oscillatory down- and up-welling bottom flows with tidal or sub-tidal frequencies strongly increase their intensity along the axis of several well-studied submarine canyons, most of them located on the North Atlantic and North Pacific margins (Xu, 2011; Puig et al., 2013; Li et al., 2019).

The Bay of Biscay shelf break, and canyons/corrugations along it, are energetic internal tide generators (Vlasenko et al., 2014). Internal tides, generated at the shelf break by across-slope tidal flows (Aslam et al., 2018 and references therein), have been observed as a coherent signal in the internal wave field up to 170 km onto the Celtic Sea shelf (Inall et al., 2011).

A high-resolution numerical simulation of the M_2 internal tide in the Whittard Canyon (Aslam et al., 2018) suggests that the depth-integrated internal tide energy flux is highly variable within the canyon and that the eastern branch, plus Explorer Canyon, Dangeard Canyon and the flanks of Brenot Spur (Fig. 1) are key generation sites. The internal tide is topographically steered along the canyon branches, but energy fluxes are directed both up- and down-canyon, depending on the branch in question (Amaro et al., 2016; Hall et al. 2017; Aslam et al., 2018). Close to the Whittard sandwave field, a hydrographic mooring time-series accompanied by a fine-resolution 3D numerical model simulation have revealed internal waves propagating north-east towards the continental shelf each semi-diurnal tidal cycle together with internal solitary waves with

up to 105 m wide amplitudes (Vlasenko et al., 2014). In Whittard Canyon itself, near-bed flows are dominated by moderate to strong semi-diurnal tidal currents orientated along the canyon axis (van Weering et al., 2000; Amaro et al., 2016). Ocean glider and hydrographic mooring time-series along the eastern tributary canyon have resolved large-amplitude (up to 150 m in height) semi-diurnal internal tides (Hall et al., 2017; Dr Furu Mienis, NIOZ, pers com; Fig. 11), possibly transitioning to asymmetrical-shaped internal bores during spring tide (Hall et al., 2017). Therefore, we postulate that internal tides are the responsible mechanism for up-slope sediment transport at the canyon head, and up-slope sandwave orientation observed on the Whittard outer shelf. Our results confirm the long-term persistence of overflowing bottom currents on the Whittard Canyon heads (Fig. 11). The net sediment transport direction is the result of a complex interplay between seafloor geomorphology and local hydrodynamics, consisting of internal tides, surface tidal residual currents and gravitational currents. The semi-diurnal internal tides interact with the rough geomorphology of the canyon head and of the surrounding steep walls, and may generate strong up-slope propagating internal bores. Geomorphological evidence indicates that the effect of up-slope internal waves is almost entirely dissipated on the outer shelf at the depth of 195 m, at a distance of 5.5 km from the western tributary head (Fig. 3, 11). The reason for which up-slope sandwaves are absent in the outer shelf adjacent to the eastern tributary is probably due to the depth-constrained action of internal waves in this specific part of the canyon. The eastern tributary cuts further into the shelf than the western tributary, giving place to the abrupt morphology of the head up to a depth of 195 m (Fig. 11). The few symmetric and up-slope sandwaves in front of the eastern tributary (Fig. 3) may represent the last remnants of an old up-slope asymmetric field, which is now totally removed through the retrogressive erosion of the canyon.

5.3 Ongoing dynamics of the Whittard Canyon sandwaves

There is a clear spatial variability of the contemporary sediment dynamics acting on the Whittard Canyon sandwaves. The contrasting asymmetric patterns of the western and eastern fields are consistent from cm to km scales, spanning ephemeral ripples to megaripples and long-lived sandwaves (Fig. 8). This finding reveals a persistent regional hydrodynamic regime, most probably controlled by the large-scale geomorphology of the Whittard Canyon.

We assume that sandwaves were more active during previous lower sea level stages, reflecting sediment dynamics and geomorphic patterns influenced by storm-induced and tide-induced bottom currents, which during the last sea level rise progressively became subordinate to the effect of the up- and down-slope flows, which currently dominate the outer shelf. At the present time, the depth of the sandwaves prevents the significant influence of storms, as observed in the nearby English Channel and North Sea deeper than 80 m (e.g., Van Landeghen et al., 2012).

On a decadal perspective, comparative MB datasets collected 15 years apart (2000-2015) do not suggest any measurable migration of sandwaves (Fig. S4). Carlson et al. (1984) estimated an average migration rate of roughly 1 cm/yr for the sandwaves observed on the head of the Navarinsky Canyon, which in our datasets would result in sub-metric migrations below the spatial resolution of our hull-mounted MB dataset (Fig. S4).

Although the Whittard Canyon sandwaves are apparently static on a metric scale, the study area can be considered as a dynamic environment. The distribution of ripples and megaripples, the observed changes in sediment composition and in the distribution of

benthic communities allowed some of the small-scale processes contributing to their slow migration to be inferred.

- The sand peaks at the head of the western tributary are entirely constituted of winnowed medium sands without any internal structure for the first 80 cm (VC_129) (Fig. 9), suggesting the recent action of strong near-bottom flows. Fresh up-slope asymmetric ripples superimposed on the peaks and the absence of any fauna (Fig. 10a), unable to settle on sediments undergoing high physical disturbance, is a further indication of recent strong hydrodynamics around the canyon heads.

- On the sandwaves stoss sides, the 40 cm thick upper sandy sheet laying on armoured bioclastic gravels and sands (VC_131-1, Fig. 9) currently represents the most dynamic component of the sandwaves, moving over relict deposits through the migration of megaripples, that have a similar height of 50-60 cm. Migration of ripples and megaripples is known to influence the dynamics of the larger sandwaves they superimpose (Naqshband et al., 2014).

- Sediment dynamics become more intense near the sandwave crests, which are exclusively composed of winnowed coarse sands, with fresh asymmetric ripples and bowl-shaped depressions over a seafloor deprived of any macrobenthic fauna (BC_ 147 - Figs. 9b, 10c, d). This observation is coherent with the role of crests in enhancing and steering bottom currents along them (Smyth, 2016). In parallel, the crest area is characterized by the absence of any benthic fauna which, similarly to what was observed on the sand peak, are probably unable to settle on a habitat dominated by strong bottom current regimes (Figs. 10c, d). The SSS mosaic at the eastern site (Fig. 6) also supports an interpretation of higher current strengths around the sandwave crests, where megaripples are

focussed (Figs. 6, 7), generally increasing in density down-slope, towards the canyon head (Figs. 7c, d).

On the other hand, several observations illustrate that the sediment dynamics is discontinuous in space and time. The accumulation of a 3 cm thick muddy layer on some sectors of the sandwave stoss sides (Fig. 9) reflects recent bedform inactivity in this area. This is further evidenced by the occurrence of faded ripples and mobile benthic fauna, which tolerate the action of medium to slow current regimes alternating with isolated physical disturbance events (Harris, 2014) (Fig. 10b). In addition, at a distance of 30 m ahead of the crest, the trough consists of bioturbated sandy sediments within a reduced muddy matrix, reflecting a lower energy environmental setting (BC_148, VC_131-2, Fig. 9). This is confirmed by faded ripples observed in the area and by the occurrence of several sessile organisms (mainly anemones) colonizing the seafloor (Fig. 10e). Preserved bioturbation structures and the homogeneous sedimentary facies within the first 40 cm of the trough sub-surface (Fig. 9) further suggests a period of stability and constant low-energy hydrodynamics persisting in this region over long-term period, with an estimated temporal scale of at least several hundreds to a few thousand years (Buffoni et al., 1992). The morpho-sedimentary characteristics shown by the eastern SSS mosaic support a similar interpretation, with higher current strength around the sandwave crests, where megaripples are focussed, and an increasing density down-slope, towards the canyon head. Low backscatter facies along most of the lee sides of both western and eastern fields most probably confirm that fine sediments dominate these sectors, which are sheltered by the strong currents crossing the crests in up- and downslope directions respectively (Figs. 4, 5b,c,d, 6, 7b). The strongest hydrodynamics acting on the Whittard Canyon sandwaves are concentrated at the canyon heads and the tallest crests and extend to the stoss sides only during the most

503 energetic events. Nonetheless, only the uppermost deposits of the sandwaves interact
504 with ongoing hydrodynamics and can promote bedform migration, whereas the deepest
505 and older sediment most likely consists of inactive and relict deposits, as already
506 described in other outer shelf settings (Goff and Duncan, 2012; Duran et al., 2018).
507 Finally, open-source EMODNET (European Marine Observation and Data Network)
508 bathymetric maps show that sandwave fields are largely present on most of the canyon
509 heads of the Celtic Margin. Although the low spatial resolution of these datasets does
510 not allow for clear quantification of sandwave asymmetry, semi-diurnal internal tides
511 are potentially an important process for enhancing up-slope sediment transport across
512 the shelf-edge of the entire Celtic margin, as already observed by Heathershaw and
513 Codd, 1985, and may be a dominant mechanism on regional scale.
514
515 **5.4 Bowl-shaped depressions: new findings on complex morpho-sedimentary**
516 **patterns along sandwave crests**
517 Fine scale AUV-SSS mosaics unveiled for the first time the bowl-shaped depressions.
518 These newly discovered morphologic features are present on most of the tallest crests of
519 the up-slope migrating sandwaves imaged in this study (Figs. 4, 5b). We hypothesize
520 that the sandwave crests on which two coexisting megaripples occur (Figs. 6, 7a, b)
521 most likely represent a precursor stage of the morpho-sedimentary process having the
522 bowl-shaped depressions as end-members (Fig. 12). The "two-fold" crest-trough-crest
523 morphology was observed on most of the eastern sandwaves (Fig. 6, 7b) and on sectors
524 of the western field, such as the crests of smaller secondary sandwaves and far from the
525 shelf-edge, which probably represent lower energy hydrodynamics (Figs. 4, 12a).
526 Megaripples around the sandwave crests can increase their sinuosity in response to local
527 hydrodynamic forcing, organize themselves in antithetic geometry, and create circular

to elongated tear-drop lobes stretched along the direction of crests (Figs. 7a, 12b, c). When two antithetic megaripples merge, possibly under persisting and stronger hydrodynamic conditions, they isolate residual portions of the troughs, generating regular patterns of rounded bowl-shaped morphologies up to 0.6 m deep (Figs. 12d, e). Assuming that megaripple trains migrate obliquely towards the sandwave crest, the wavelength of megaripples and their orientation are responsible for the dimensions of the bowl-shaped features, which resemble megaripples in both wavelength and height.

Despite these intriguing geomorphologies having never being observed in subaqueous settings, similar spatial patterns have been described on the crests of terrestrial and martian aeolian dunes controlled by bi-directional winds (Parteli et al., 2009; Courrech du Pont et al., 2014). Meandering and antithetic dune crests occur under the alternate action of oblique winds with divergence angles larger than 90° (Parteli et al., 2009; Gadall et al., 2019). Under these conditions, bedforms align with the dominant direction of the two flows, optimizing the maximum gross sediment transport able to maintain them (Rubin and Hunter, 1987; Courrech du Pont et al., 2014; Gadal et al., 2019). Bottom currents may increase their maximum bed shear stress approaching the crests of the sandwaves, and steer secondary flows directed in the ebb direction (Gadall et al., 2019), which could explain the along-crest elongation of some bowl-shaped depressions (Fig. 11b). Moreover, field observations and 3D Computational Fluid Dynamics (CFD) hint at an increased undulation of (sandwave) crest line and the action of oblique winds as dominant parameters in producing deflected reverse flows, forming stretched corkscrew vortices parallel to the dune (Delgado-Fernandez 2013; Jackson et al., 2013; Smyth, 2016).

The bowl-shaped depressions around the head of the Whittard Canyon only develop on the crests of the tallest sandwaves (Fig. 4), suggesting the crucial role of sandwave

height which, as observed on sub-aerial settings, can alter local hydrodynamics producing higher energetic regimes around the crests (Smyth, 2016; Gadal et al., 2019). Where bowl-shaped depressions occur, morphologic evidence resembles some of the above mentioned pre-conditioning factors, with megaripples producing a rough undulation of the sandwave crest line and their orientation (the assumed direction of primary flows - red arrow in Fig. 12d) forming angles from 60° to 120° with the sandwave crests (the assumed direction of secondary flows - blue arrow in Fig. 12d). Nonetheless, without the acquisition of repeated mapping and long hydrodynamic time-series, and an awareness that subaqueous and subaerial mechanisms may yield substantial differences, a definitive understanding of the dynamics related to these features still remains unclear and speculative.

6. CONCLUSIONS

The application of multiple resolution geophysical mapping, including cutting-edge marine robotics, unveiled uncommon up- and down-slope active bedform fields at the head of the Whittard Canyon, displaying variability in intensity and direction of sediment transport within a few hundreds of meters. The bedforms recognized in the study area are sandwaves, megaripples, ripples, original sand peaks, and newly discovered features along the sandwave crests, such as two-fold crests, tear-drop lobes and bowl-shaped depressions.

Hydrodynamics inferred from asymmetric patterns of bedforms is consistent from cm (ripples) to m (megaripples) and km (sandwaves) scales, suggesting a persistent regime in the area maintained by the large-scale geomorphology of the Whittard Canyon head.

Large-amplitude semi-diurnal internal tides transitioning to asymmetric internal bores under near-critical reflection, are the suspected mechanisms for the generation of strong up-canyon bottom currents, deduced to be up to 1 m/s, overflowing the canyon rim to the outer shelf and generating up-slope bedform fields in the outer shelf deeper than 190 m. Shallower, up-slope currents generated in the canyon lose intensity, and downslope bedforms fields are preferentially developed.

Based on fne-scale observations, the strongest hydrodynamics, able to produce sediment transport, are concentrated at the heads of the two studied tributary canyons and at the tallest sandwave crests, where spectacular trains of bowl-shaped depressions, never observed before, suggest self-organizing patterns of megaripples, in response to bi-directional current regimes interacting with a complex geomorphology.

Nonetheless, only the uppermost sediments of the sandwaves promote ongoing bedform activity through ripples and megaripples migration, whereas the deepest sediments seem to remain inactive as relict deposits.

Our results demonstrate the paramount importance of high-resolution methodologies in the study of deep water settings like active bedform fields, yielding relevant insights on the dynamics of complex environments, with implications in geo-hazard assessment for industrial infrastructures and exchange of carbon-rich particles across shelf/slope fronts.

7. ACKNOWLEDGEMENTS

Most of the data used in this work has been acquired in the JC125 cruise, funded by the

ERC CODEMAP project (Complex Deep-sea Environments: Mapping habitat heterogeneity As Proxy for biodiversity) (Grant No. 258482, PI: Dr V.A.I. Huvenne). Additional data have been collected in the frame of the NERC funded CLASS programme, Grant No. NE/R015953/1. We acknowledge the captain and crew of the RRS James Cook for their assistance during the JC125 and JC166 expeditions. Special thanks go to Tim Le Bas for processing the AUV-SSS and AUV-MB maps, and to the ROV "ISIS" team for their kind cooperation during data acquisition. The 2000 MB dataset has been collected in the frame of the INFOMAR project (Integrated Mapping for the Sustainable Development of Ireland's Marine Resources). We are finally indebted with Dr P. Puig, for the fruitful discussions we had during the production of this work, and with Dr. F. Mienis for her kindness in sharing information on hydrographic mooring time-series. Gareth Carter publishes with permission of the Director of the British Geological Survey (United Kingdom Research and Innovation).

8. REFERENCES

Ahmerkamp, S., Winter, C., Janssen, F., Kuypers, M.M.M., Holtappels, M., 2015. The impact of bedform migration on benthic oxygen fluxes. J. Geophys. Res. 120, 2229–2242. doi:10.1002/2015JG003106.

Amaro, T., Huvenne, V.A.I., Allcock, A.L., Aslam, T., Davies, J.S., Danovaro, R., De Stigter, H.C., Duineveld, G.C.A., Gambi, C., Gooday, A.J., Gunton, L.M., Hall, R., Howell, K.L., Ingels, J., Kiriakoulakis, K., Kershaw, C.E., Lavaleye, M.S.S., Robert, K., Stewart, H., Van Rooij, D., White, M., Wilson, A.M., 2016. The Whittard Canyon – a case study of submarine canyon processes. Prog. Oceanogr. 146, 38–57.

627 Allen, S.E., Durrieu de Madron, X., 2009. A review of the role of submarine canyons in
628 deep-ocean exchange with the shelf Ocean Sci., 5, 607–620,. www.ocean-
629 sci.net/5/607/2009/
630
631 Aslam, T., Hall, R. A., Dye, S. R., 2018. Internal tides in a dendritic submarine canyon.
632 Progress in Oceanography 169, 20-32. doi:10.1016/j.pocean.2017.10.005.
633
634 Azpiroz-Zabala, M., Cartigny, M.J.B., Talling, P.J., Parsons, D.R., Sumner, E.J., Clare,
635 M.A., Simmons, S.M., Cooper, C., Pope, E., 2017. Newly recognized turbidity current
636 structure can explain prolonged flushing of submarine canyons. Science advances 3-10,
637 doi: 10.1125/sciadv1700200
638
639 Berné, S., Laricolais, G., Marsset, T., Bourillet, J.F., De Batist, M., 1998. Erosional
640 offshore sand ridges and lowstand shorefaces: examples from tide- and wave-dominated
641 environments of France. Journal of Sedimentary Research 68, 540-555.
642
643 Bouysse, P., Horn, R. Lapierre, F., Le Lann, F., 1976. Etude des grands bancs de sable
644 du sud-est de la Mer Celtique, Marine Geology 20, 251-275.
645
646 Bourillet, J.F., Zaragosi, S., Mulder, T., 2006. The French Atlantic margin and deep-sea
647 submarine systems. Geo-Marine Letters 26, 311–315.
648
649 Buffoni, G., Delfanti, R., Papucci, C., 1992. Accumulation rates and mixing processes
650 in near-surface North Atlantic sediments: Evidence from C-14 and Pu-239,240
651 downcore profiles. Marine Geology 109 (1-2), 159-170.

652

653 Carlson, P.R, Fischer J.M., Karl, H.A., Larrdn, C., 1984. Isopach map of Seismic Unit
654 A, youngest sedimentary sequence in Navarin basin, in Karl, H. A., and Carlson, P. R.,
655 eds., Surface and Near-Surface Geology, Navafin Basin Province: results of the 1980-
656 81 field seasons: U.S. Geol. Survey Open-File Report 84-89, p. 33-38.

657

658 Carter, G.D.O., Huvenne, V.A.I., Gales, J.A., Lo Iacono, C., Marsh, L., Ougier-
659 Simonine A., Robert, K., Wynn, R.B., 2018. Ongoing evolution of submarine canyon
660 rockwalls; examples from the Whittard Canyon, Celtic Margin (NE Atlantic). Progress
661 in Oceanography 169, 79-88. doi: 10.1016/j.pocean.2018.02.001.

662

663 Courrech du Pont, S., Narteau, C., Gao, X., 2014. Two modes for dune orientation.
664 Geology 42-9, 743–746.

665

666 Cunningham, M.J., Hodgson, S., Masson, D.G., Parson, L.M., 2005. An evaluation of
667 along-and down-slope sediment transport processes between Goban Spur and Brenot
668 Spur on the Celtic Margin of the Bay of Biscay. Sedimentary Geology 79-1, 99–116.

669

670 Dauxois, T., Young W.R., 1999. Near Critical Reflection of Internal Waves. Journal of
671 Fluid Mechanics 390. doi: 10.1017/S0022112099005108.

672

673 Delgado-Fernandez, I., Jackson, D.W.T., Cooper, J.A.G., Baas, A.C.W., Beyers, J.H.,
674 Lynch, K., 2013. Field characterization of three-dimensional lee-side airflow patterns
675 under offshore winds at a beach-dune system. Journal of Geophysical Research - Earth
676 Surface 118, 706–721.

Durán, R., Guillén, J., Rivera, J., Lobo, F.J., Muñoz, A., Fernández-Salas, L.M., Acosta, J., 2018. Formation, evolution and present-day activity of offshore sand ridges on a narrow, tideless continental shelf with limited sediment supply. Marine Geology 397, 93–107.

Gadall, C., Narteau, C., Courrech du Pont, S., Rozier, O., Claudin, P., 2019. Incipient bedforms in a bidirectional wind regime. Journal of Fluid Mechanics 862, 490-516. doi: https://doi.org/10.1017/jfm.2018.978

Goff, J.A., Duncan, L.S., 2012. Re-examination of sand ridges on the middle and outer New Jersey shelf based on combined analysis of multibeam bathymetry and backscatter, seafloor grab samples and chirp seismic data. Int. Assoc. Sedimentol. Spec. Publ. 44, 121–142.

Hall, R.A., Carter, G.S., 2011. Internal tides in Monterey Submarine Canyon. Journal of Physical Oceanography 41, 186–204. http://dx.doi.org/10.1175/2010JPO4471.1.

Hall, R.A., Aslam, T., Huvenne, V.A.I., 2017. Partly standing internal tides in a dendritic submarine canyon observed by an ocean glider. Deep Sea Research Part I 126, 73{84, doi:10.1016/j.dsr.2017.05.015.

Harris, P.T., 2014. Shelf and deep-sea sedimentary environments and physical benthic disturbance regimes: a review and synthesis. Marine Geology 353, 169–184.

Heathershaw, A.D., Codd, J.M., 1985. Sandwaves, internal waves and sediment mobility at the shelf-edge in the Celtic Sea. Oceanologica Acta 8-4, 391-404.

Hotchkiss, F.S., Wunsch, C., 1982. Internal waves in Hudson Canyon with possible geological implications. Deep-Sea Research Part I 29, 415-442.

Hopkins, J.E., Stephenson, G.R., Green, J., Inall, M.E., Palmer, M.R., 2014. Storms modify baroclinic energy fluxes in a seasonally stratified shelf sea: inertial-tidal interaction. Journal of Geophysical Research - Oceans 119, 6863–6883.

Inall, M., Aleynik, D., Boyd, T., Palmer, M., Sharples, J., 2011. Internal tide coherence and decay over a wide shelf sea. Geophysical Research Letters 38, L23607, doi:10.1029/2011GL049943.

Jackson, D.W.T., Beyers, M., Delgado-Fernandez, Irene., Baas, Andreas C.W., Cooper, A. J., Lynch, Kevin., 2013. Airflow reversal and alternating corkscrew vortices in foredune wake zones during perpendicular and oblique offshore winds. Geomorphology 187, 86–93. http://dx.doi.org/10.1016/j.geomorph.2012.12.037.

Jiang, W., Lin, M., 2016. Research on bilateral reverse migration of one-group seabed sand waves in a small shallow shelf sea. Coastal Engineering 111, 70–82.

Karl, H.A., Cacchione D.A., Carlson P.R., 1986. Internal-wave currents as a mechanism to account for large sand wave in Navarinsky Canyon head, Bering Sea. Journal of Sedimentary Petrology 56-5, 706-714.

Knaapen, M.A.F., 2005. Sandwave migration predictor based on shape information. Journal of Geophysical Research 110, F04S11, doi:10.1029/2004JF000195

Knebel, H.J., Folger, D.W., 1976. Large sand waves on the Atlantic outer-continental shelf around Wilmington Canyon, off eastern United States: Marine Geology 22, 7-I5.

Legg, S., Adcroft, A., 2003. Internal Wave Breaking at Concave and Convex Continental Slopes. Journal of Physical Oceanography 33, 2224-2246. https://doi.org/10.1175/1520-0485(2003)033<2224:IWBACA>2.0.CO;2

Li, M.Z., Prescott, R.H., Robertson, A.G., 2019. Observation of internal tides and sediment transport processes at the head of Logan Canyon on central Scotian Slope, eastern Canada. Journal of Marine Systems 193, 103–125. https://doi.org/10.1016/j.jmarsys.2019.02.007.

Lo Iacono, C., Guillén, J., Puig, P., Ribó, M., Ballesteros, M., Palanques, A., Farrán, M., Acosta, J., 2010. Large-scale bedforms along a tideless outer shelf setting in the Western Mediterranean. Continental Shelf Research 30, 1802-1813.

Mulder, T., Zaragosi, S., Garlan, T., Mavel, J., Cremer, M., Sottolichio, A., Sénéchal, N., Schmidt, S., 2012. Present deep-submarine canyons activity in the Bay of Biscay (NE Atlantic). Marine Geology 295–298, 113–127.

751 Naqshband, S., Ribberink, J.S., Hurther, D., Hulscher, S.M.J.H., 2014. Bed load and
752 suspended load contributions to migrating sand dunes in equilibrium. Journal of
753 Geophysical Research - Earth Surface 119, 1043–1063, doi:10.1002/2013JF003043.
754
755 Pantin, H.M., Evans, C.D.R., 1984. The Quaternary history of the central and
756 southwestern Celtic Sea. Marine Geology 57, 259--293.
757
758 Parker, G., 1996. Some speculations on the relation between channel morphology and
759 channel-scale flow structures, in Ashworth, P.J., et al., eds., Coherent flow structures in
760 open channels: Chichester, Wiley, p. 423–459.
761
762 Parteli, E.J.R., Durán, O., Tsoar, H., Schwämmled, V., Herrmann, H.J., 2009. Dune
763 formation under bimodal winds. PNAS December 29, 2009 vol. 106 no. 52 22085-
764 22089.
765
766 Paull, C., Caress, D.W., Ussler, W., Lundsten, E., Meiner-Johnson, M., 2011. High-
767 resolution bathymetry of the axial channels within Monterey and Soquel submarine
768 canyons, offshore central California. Geosphere 7-5, 1077–1101. doi:
769 10.1130/GES00636.1.
770
771 Pingree, R., 1980. Physical oceanography of the Celtic sea and English channel.
772 Elsevier Oceanography Series 24, 415–465.
773

774 Pingree, R.D., Sinha, B., Griffiths, C.R., 1999. Seasonality of the European slope
775 current (Goban Spur) and ocean margin exchange. Continental Shelf Research 19, 929–
776 975.
777
778 Piper, D.J.W., Normark, W.R., 2009. Processes that initiate turbidity currents and their
779 influence on turbidites: a marine geology perspective. Journal of Sedimentary Research
780 79, 347–362.
781
782 Praeg, D., McCarron, S., Dove, D., Ó Cofaigh, C., Scott, G., Monteys, X., Facchin, L.,
783 Romeo, R., Coxon, P., 2015. Ice sheet extension to the Celtic Sea shelf edge at the Last
784 Glacial Maximum. Quaternary Science Reviews 111, 107–112.
785
786 Puig, P., Greenan, B.J.W., Li, M.Z., Prescott, R.H., Piper, D.J.W., 2013. Sediment
787 transport processes at the head of Halibut Canyon, eastern Canada margin: an interplay
788 between internal tides and dense shelf-water cascading. Marine Geology 341, 14–28.
789
790 Reynaud, J.Y., Tessier, B., Berné, S., Chamley, H., de Batist, M., 1999. Tide and wave
791 dynamics on a sand bank from the deep shelf of the Western Channel approaches. Marie
792 Geology 161, 339–359.
793
794 Rovere, M., Pellegrini, C., Chiggiato, J., Campiani, E., Trincardi, F., 2019. Impact of
795 dese bottom water on a continental shelf: an example from the SW Adriatic Sea. Marine
796 Geology 408, 123-142. doi:10.1016/j.margeo.2018.12.002.
797

798 Rubin, D.M., Hunter, R.E., 1987. Bedform Aligmment in Directionally Varying Flows.
799 Science 237, 276-278.
800
801 Scourse, J., Uehara, K., Wainwright, A., 2009. Celtic Sea linear tidal sand ridges, the
802 Irish Sea Ice Stream and the Fleuve Manche: palaeotidal modelling of a transitional
803 passive margin depositional system. Marine Geology 259, 102e111.
804
805 Sharples, J., Tweddle, J.F., Mattias Green, J., Palmer, M.R., Kim, Y.N., Hickman, A.E.,
806 Holligan, P.M., Moore, C.M., Rippeth, T.P., Simpson, J.H., et al., 2007. Spring-neap
807 modulation of internal tide mixing and vertical nitrate fluxes at a shelf edge in summer.
808 Limnology and Oceanography 52, 1735–1747.
809
810 Slootman, A., Cartigny, M.J.B., 2020. Cyclic steps: review and aggradation based
811 classification. Earth-Science Reviews 201, 102949.
812 https://doi.org/10.1016/j.earscirev.2019.102949
813
814 Smyth, T.A.G., 2016. A review of Computational Fluid Dynamics (CFD) airflow
815 modelling over aeolian landforms. Aeolian Research 22, 153–164.
816
817 Southard, J.B., Boguchwal, L.A., 1990. Bed configuration in steady unidirection water
818 flows. Part 2. Synthesis. Journal of Sedimentary Petrology 60-5. 658-679.
819
820 Van Landeghem, K.J.J., Baas, J.H., Mitchell, N.C., Wilcockson, D., Wheeler, A.J.,
821 2012. Reversed sediment wave migration in the Irish Sea, NW Europe: A reappraisal of

the validity of geometry-based predictive modelling and assumptions. Marine Geology 295–298, 95–112.

van Weering, T.C.E., Thomsen, L., van Heerwaarden, J., Koster, B., Viergutz, T., 2000. A seabed lander and new techniques for long term in situ study of deep-sea near bed dynamics. Sea Technology 41, 17–27.

Vlasenko, V., Stashchuk, N., Inall, M.E., Hopkins, J.E., 2014. Tidal energy conversion in a global hot spot: on the 3-d dynamics of baroclinic tides at the Celtic sea shelf break. Journal of Geophysical Research - Oceans 119, 3249–3265.

Xu, J.P., 2011. Measuring currents in submarine canyons: technological and scientific progress in the past 30 years. Geosphere 7, 868–876.

9. FIGURE CAPTIONS

Figure 1: a) Multibeam bathymetric map of the Whittard Canyon, composed of MB data belonging to NOC, INFOMAR Project (Integrated Mapping For The Sustainable Development Of Ireland's Marine. Resource Programme.- Marine Institute and Geologic Survey of Ireland) and EU Emodnet Project (European Marine Observation and Data Network - Bathymetry Data Portal). EC: Explorer Canyon. DC: Dangeard Canyon; b) bedform fields presented in this study, mapped at the heads of two tributary canyons of the Whittard eastern branch (western and eastern tributaries). Ellipsoid projection: WGS84.

Figure 2: Schematic representation and nomenclature of the sandwave characteristics used in this study: L, wavelength; L1 and L2, lee and stoss side wavelength, respectively; h, dune height (with slope correction); Zc, crest depth; Z1 and Z2, trough depth; Xc, X1 and X2, position of the sandwave crest and troughs along the bathymetric profile; α, slope angle.

Figure 3: Asymmetry indexes of the Whittard Canyon sandwaves, classified in upslope asymmetric (red, AI < -0.25), symmetric (white, -0.25 < AI < 0.25), and downslope asymmetric (blue, AI > 0.25). Black dashed lines indicate the tracks of bathymetric profiles illustrated in panels 1 and 2. Arrows in bathymetric profiles reflect the direction of sediment transport deduced by sandwave asymmetry and the colour of asymmetry classes. Ellipsoid projection: WGS84.

Figure 4: 15 cm grid cell resolution AUV-SSS mosaic acquired on the western field sandwaves. Lighter shades correspond to higher backscatter. The white dashed line coincides with the track of the below bathymetric profile. Numbers indicate the major sandwaves of this sector.

Figure 5: Enlargements of the western AUV-SSS mosaic (Figure 4) and corresponding bathymetric profiles (yellow dashed lines). Lighter shades correspond to higher backscatter. Orange dashed lines in 5a indicate the longitudinal axes of numbered sand peaks. bsd in c and c1: bowl-shaped depression. BS in b and d: backscatter. Low BS acoustic facies are observed in figures b, c and d on the lee side and part of the trough, likely indicating fine sediment areas, sheltered by strong upslope bottom currents. Locations shown in Figure 4.

871

872 **Figure 6**: 15 cm grid cell resolution AUV-SSS mosaic acquired on the eastern field
873 sandwaves. Lighter shades correspond to higher backscatter. The white dashed line
874 coincides with the track of the below bathymetric profile. Numbers indicate the major
875 sandwaves of this sector.

876

877 **Figure 7**: Enlargements of the eastern AUV-SSS mosaic (Figure 6) and corresponding
878 bathymetric profiles (yellow dashed lines). Locations shown in Figure 6. High and low
879 backscatter (BS) acoustic facies are observed on the stoss and lee side of figure 7b,
880 likely indicating coarse vs fine sediment areas, respectively exposed to and sheltered by
881 downslope bottom currents.

882

883 **Figure 8**: Vectors of sediment transport direction deduced from sandwave (white
884 arrows) and megaripple (orange arrows) asymmetry. Criteria for defining asymmetric
885 trends are the same adopted in Figure 3. Density of megaripples (exclusively occurring
886 where orange arrows are depicted) increase downslope, towards the heads of both
887 western and eastern tributaries. Symmetric megaripples are more numerous in the
888 eastern field, likely evolving under the bidirectional action of tidal currents at the
889 bottom.

890

891 **Figure 9**: Enlargements of the AUV-SSS mosaic of western field (locations in Figure 4)
892 showing in a): the sand peak where the ROV-vibro-core VC_129 (red dot) was
893 retrieved; in b): the sandwave where the ROV-vibro-cores VC_131-1, VC_131-2
894 (orange and green dots, respectively) and the box-cores BC_147, BC_148 (dark and
895 light blue, respectively) were retrieved. BS stands for backscatter. Lighter shades
896 correspond to higher backscatter. Red crosses correspond to the location of ROV

images showed in Figure 10. Yellow dashed lines correspond to the tracks of the below bathymetric profiles. Numbers in (a) correspond to the crests along the peaks. The bathymetric profile of (b) coincides with the track of the ROV dive during which the vibro-cores were collected. Arrows on bathymetric profiles coincide with the location of retrieved samples. Below graphs show granulometric composition and photos of the cores.

Figure 10: Bathymetric profiles (same tracks of Figure 9) and video-images from ROV dives on the sampled sand peak (a; Figure 9a), and on the stoss (b) crest (c, d) and trough (e) of the sampled sandwave (Figure 9b). Figures 10 a, b and e correspond to the exact locations where VB129, 131-1 and 131-2 have been collected respectively.

Figure 11: 3D bathymetric sketch illustrating the main hydrodynamic and sedimentary processes occurring in the study area. Up-slope bottom currents dominate the outer shelf adjacent to the western tributary for a depth range of 190-220 m, whereas the eastern tributary, carving the outer shelf for this depth range, is dominated by downslope currents, being channelized within the gullies of the canyon head. Dots on the eastern canyon axis correspond to the locations where an ocean glider (red dot, Hall et al., 2017) and a hydrographic mooring (yellow dot, Dr Furu Mienis, pers. comm.) resolved large-amplitude semi-diurnal internal tides.

Figure 12: Proposed evolutionary model of bowl-shaped depressions, originating from megaripples crests laying on sandwave crests (two-fold crests, a) under the action of bi-directional current regimes, transitioning to tear-drop lobes (b, c) and to bowl-shaped depressions (d), regularly spaced along the sandwave crests (e). Red arrow indicates the

direction of dominating bottom currents, deduced from megaripple orientation; blue arrow indicates the orientation of secondary currents, generated from the interaction of current flows with the articulated morphology of sandwave crests. Lighter shades correspond to higher backscatter.

Figure S1: Morphometric characteristics (wavelength, height and asymmetry) of the Whittard Canyon sandwaves.

Figure S2: 25 cm grid cell resolution AUV-MB map of the eastern sandwave field.

Figure S3: Morphometric characteristics (wavelength, height and asymmetry) of the sandwaves of western and eastern field.

Figure S4: Sandwave migration rates obtained by comparing two bathymetric grids acquired 15 years apart. Note that the comparative 2000 MB grid used to estimate potential migration has a pixel resolution of 15 m. Migrations within a distance of around 20 m, corresponding to up around 90% of measurements, are therefore considered as bias, and not taken into consideration. Estimates of rates larger than 20 m are considered as artefacts.

Figure1_Lo Iacono et al., 2019
Click here to download high resolution image

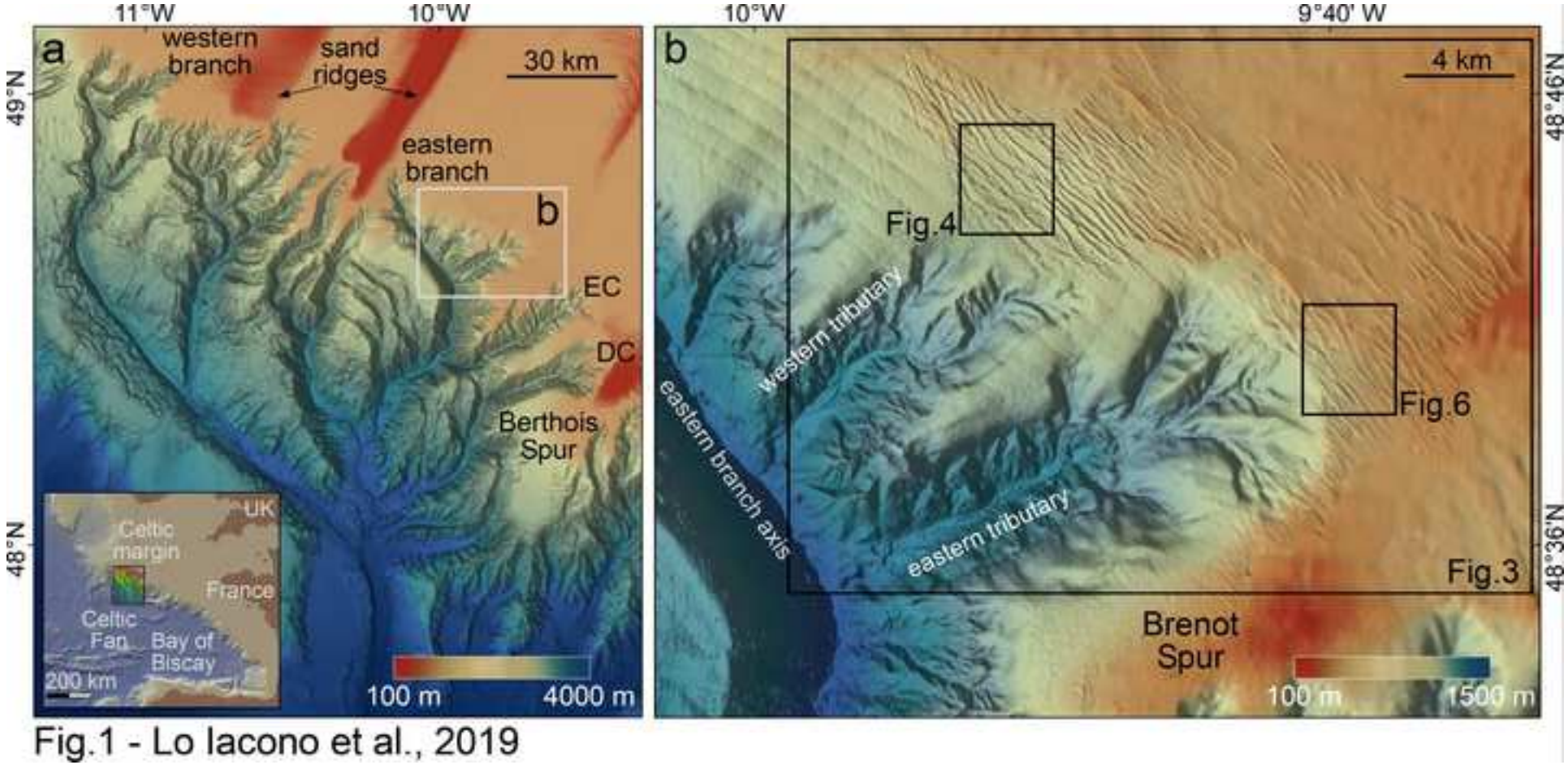

Fig.1 - Lo Iacono et al., 2019

Figure2_Lo Iacono et al., 2019
Click here to download high resolution image

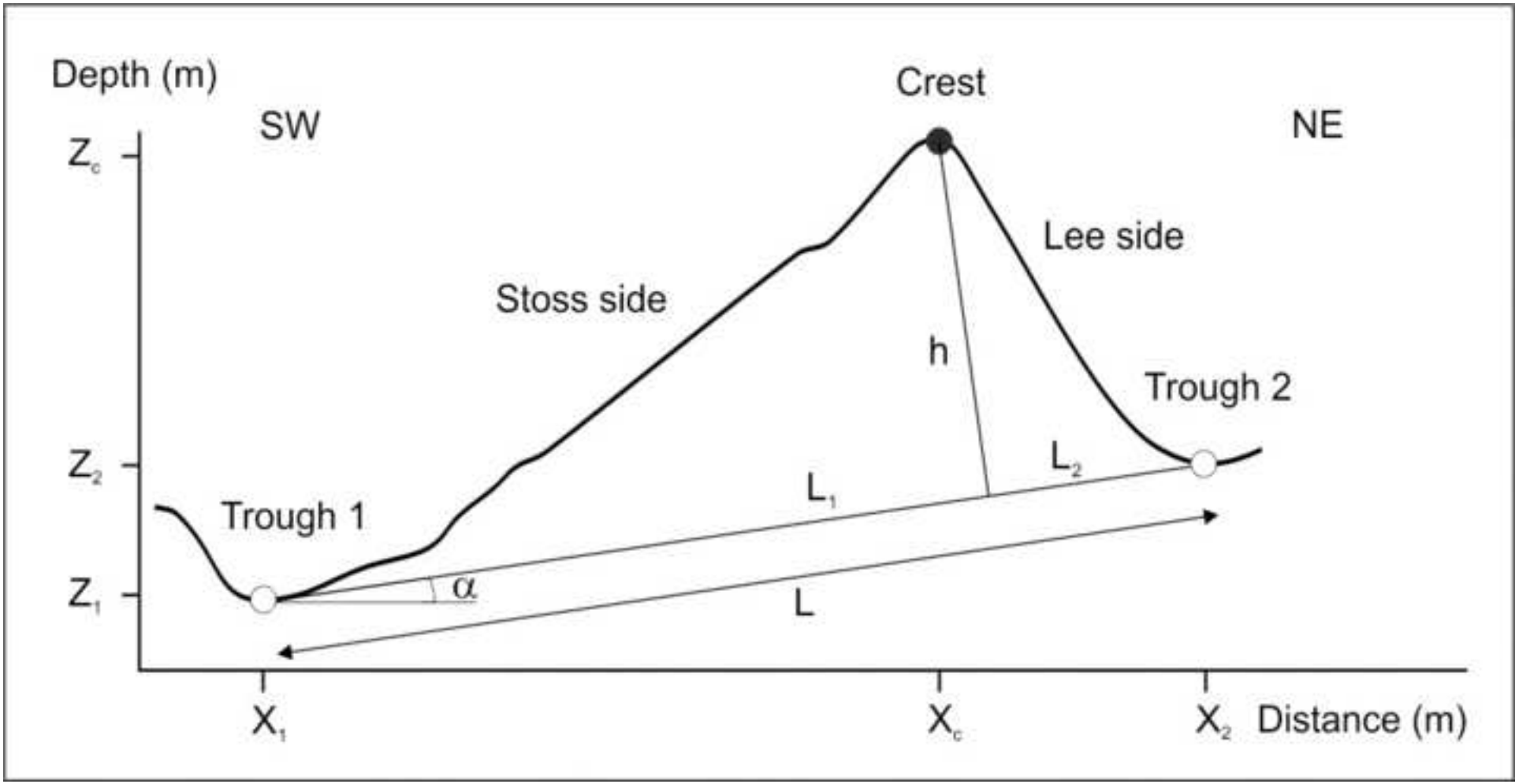

Figure3_Lo Iacono et al., 2019
Click here to download high resolution image

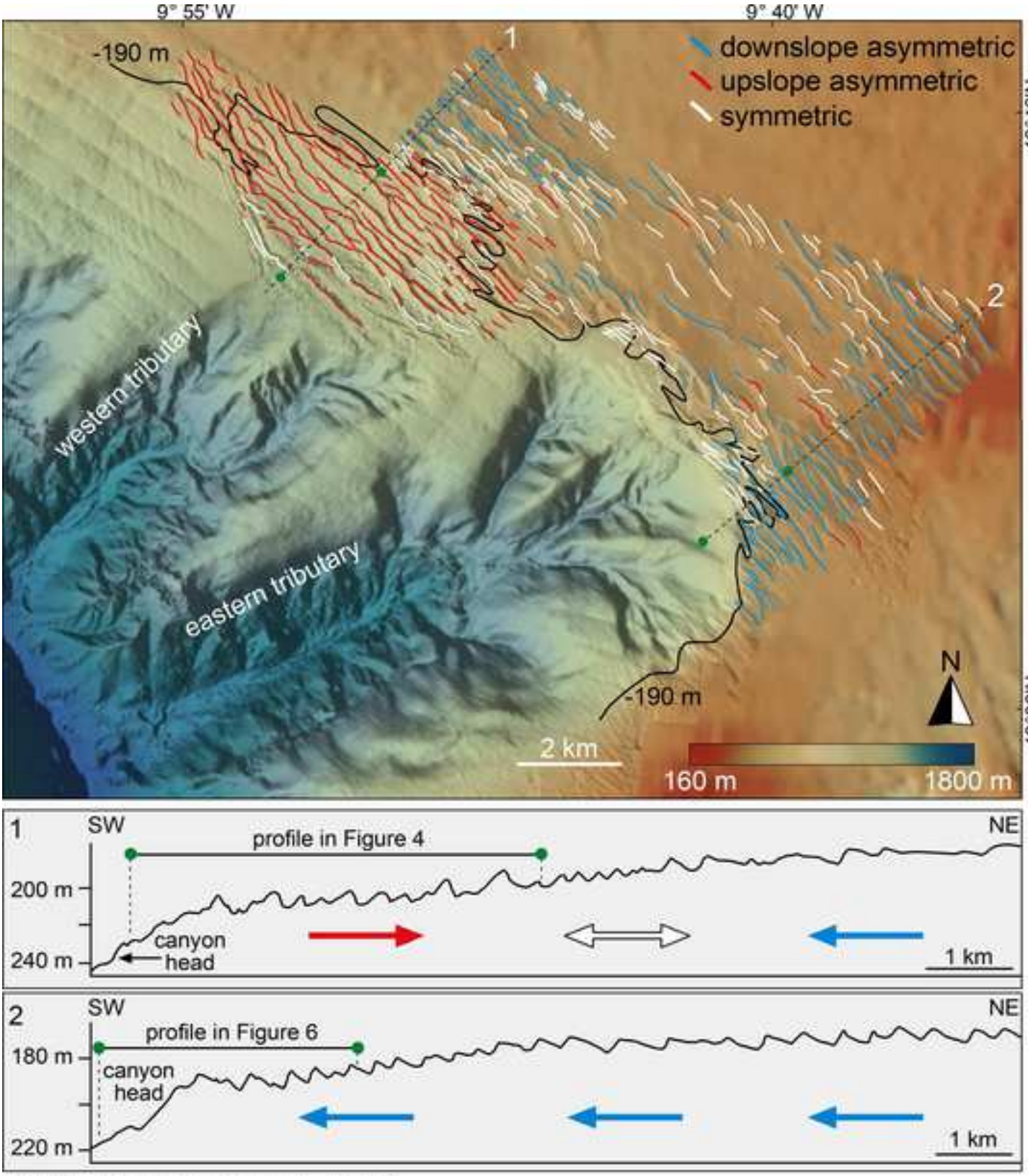

Fig.3 - Lo Iacono et al., 2019

Figure4_Lo Iacono et al., 2019

Click here to download high resolution image

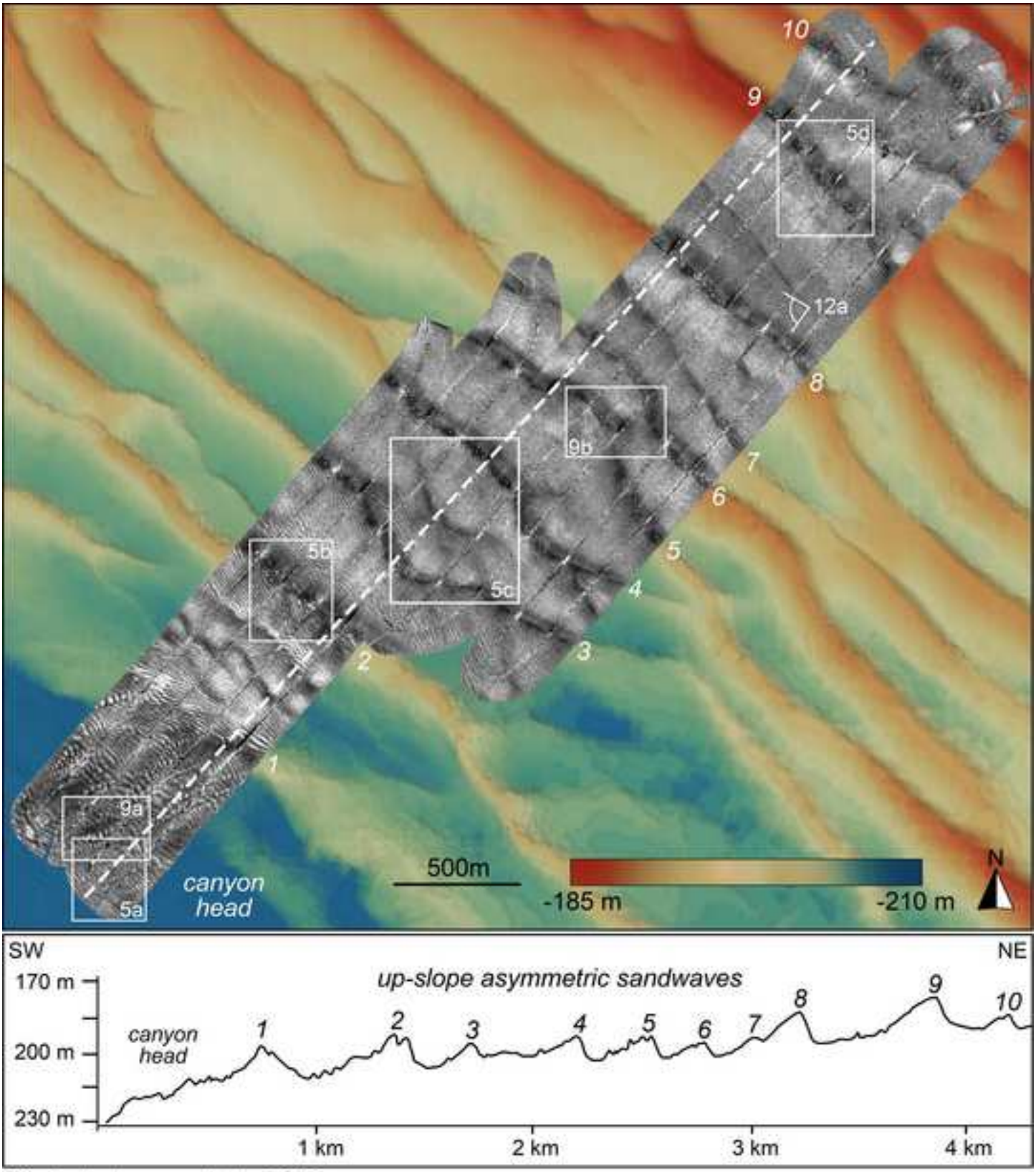

Fig.4 - Lo Iacono et al., 2019

Figure5_Lo Iacono et al., 2019

Click here to download high resolution image

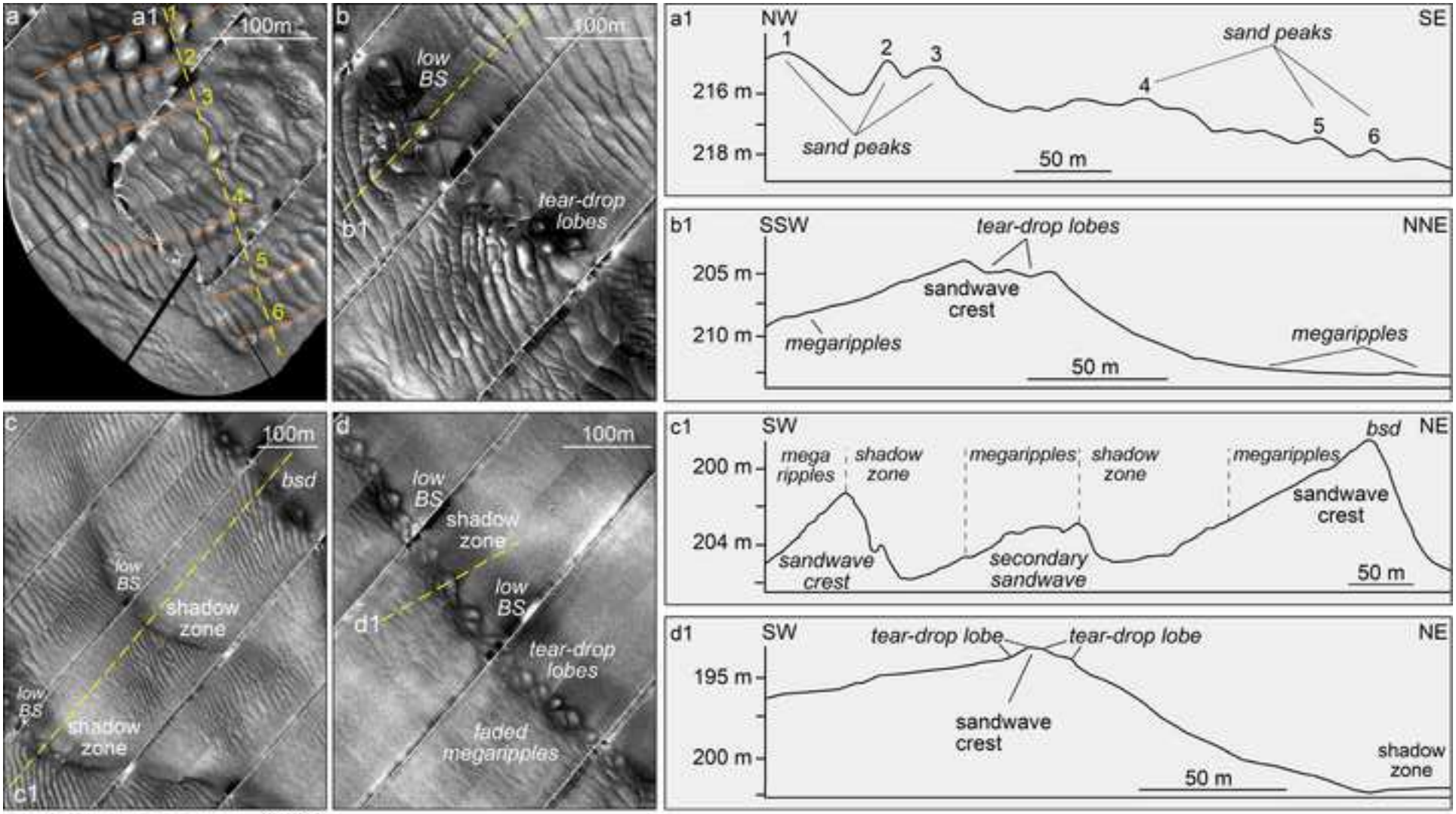

Fig.5 - Lo Iacono et al., 2019

Figure6_Lo Iacono et al., 2019
Click here to download high resolution image

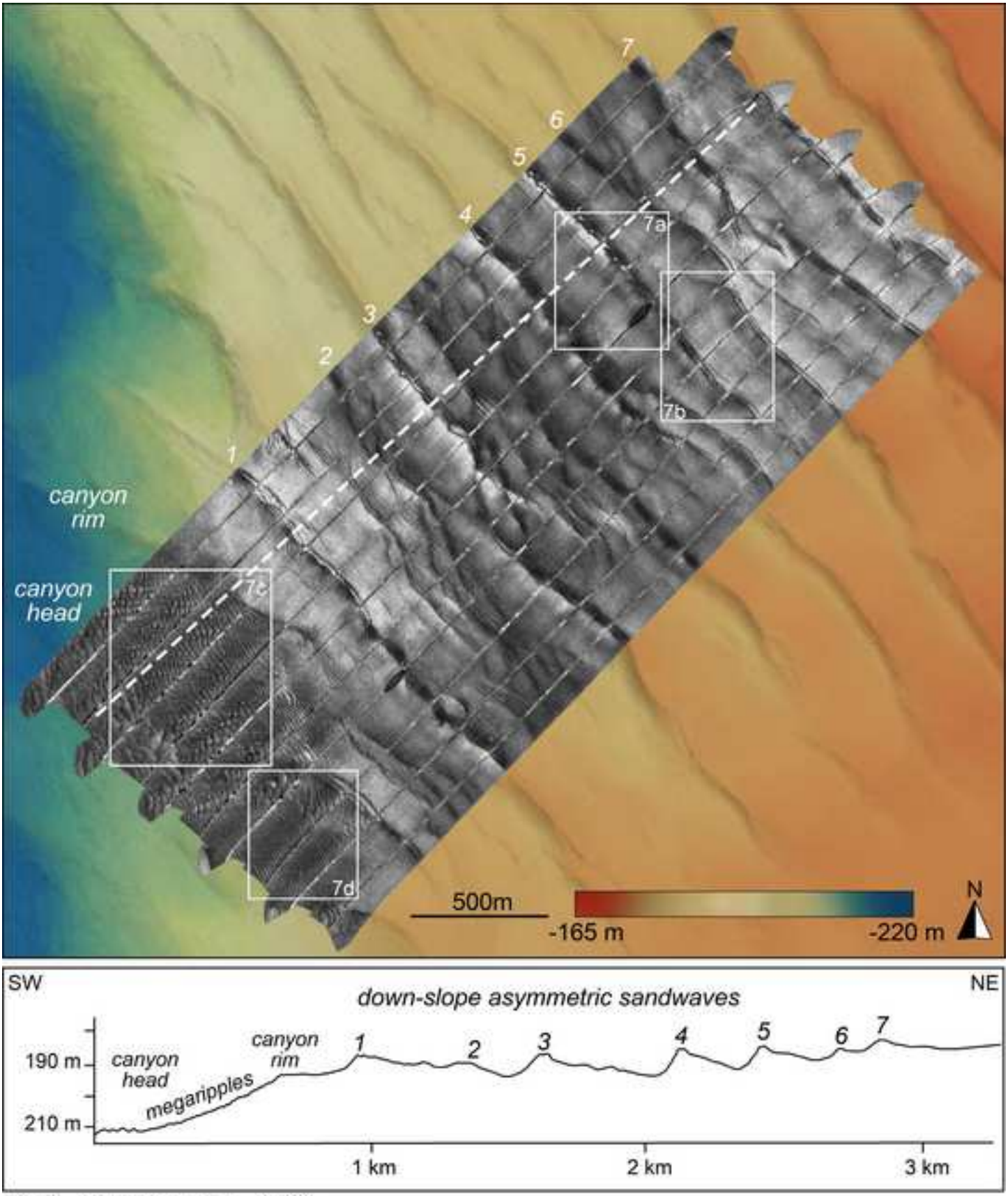

Fig.6 - Lo Iacono et al., 2019

Figure7_Lo Iacono et al., 2019

Click here to download high resolution image

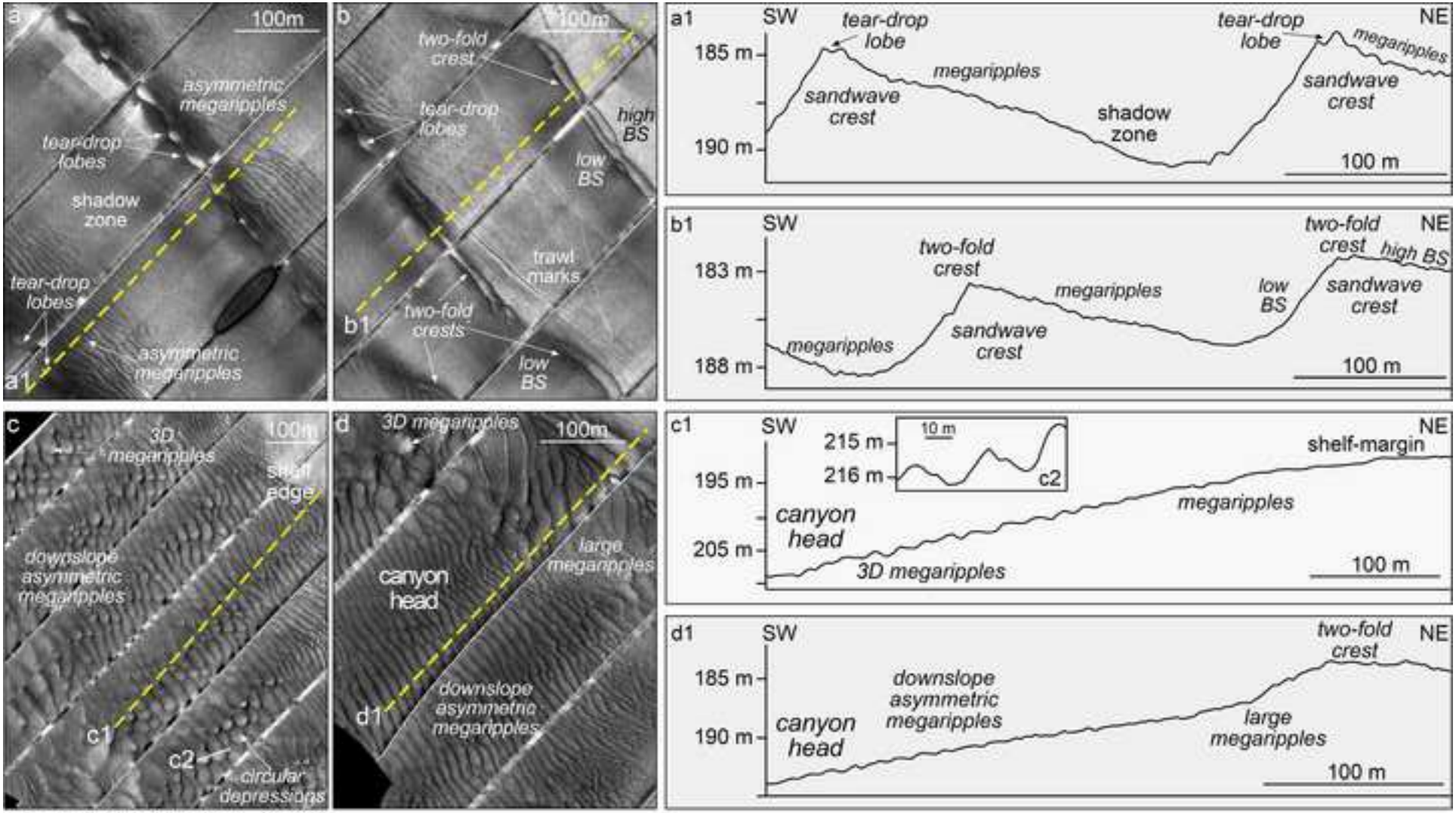

Fig.7 - Lo Iacono et al., 2019

Figure8_Lo Iacono et al., 2019
Click here to download high resolution image

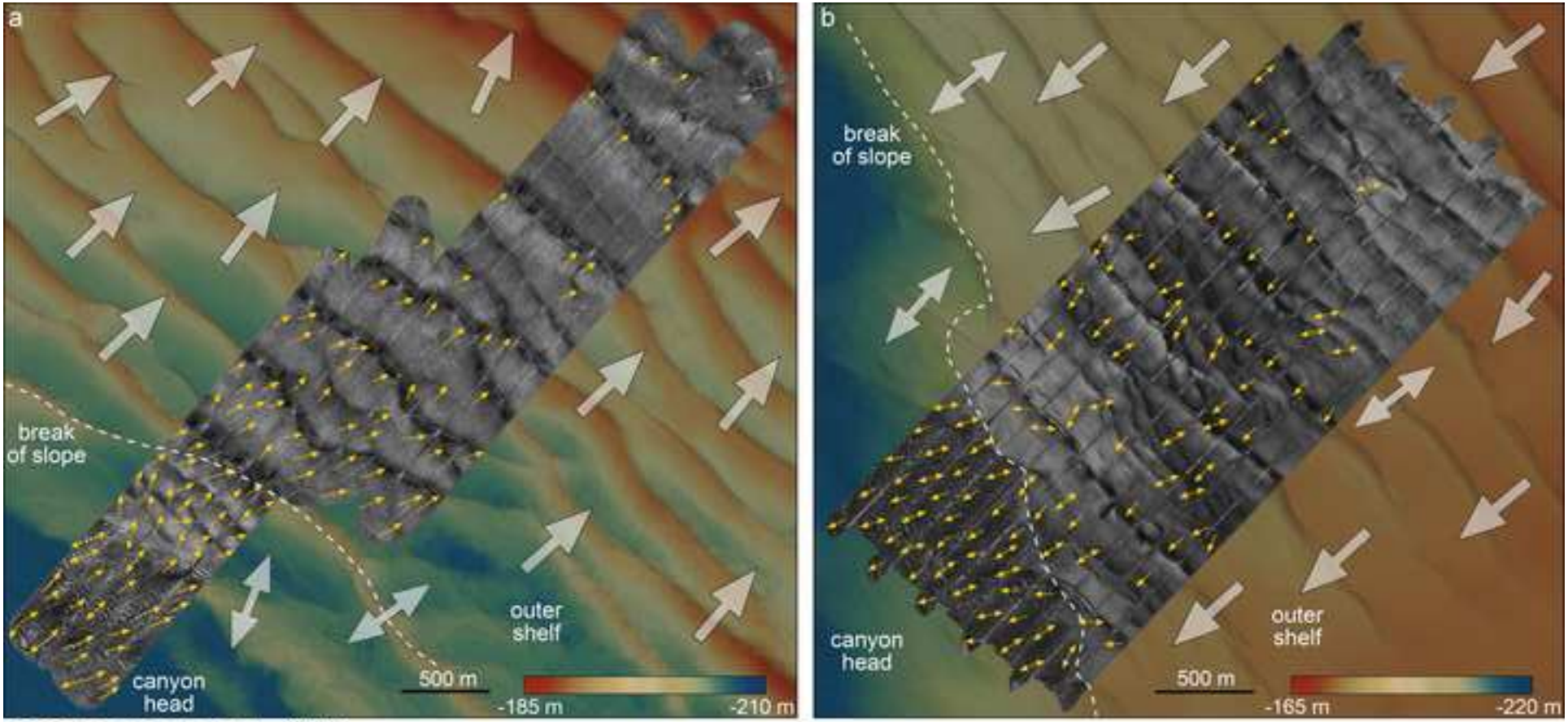

Fig.8 - Lo Iacono et al., 2019

Figure9_Lo Iacono et al., 2019

Click here to download high resolution image

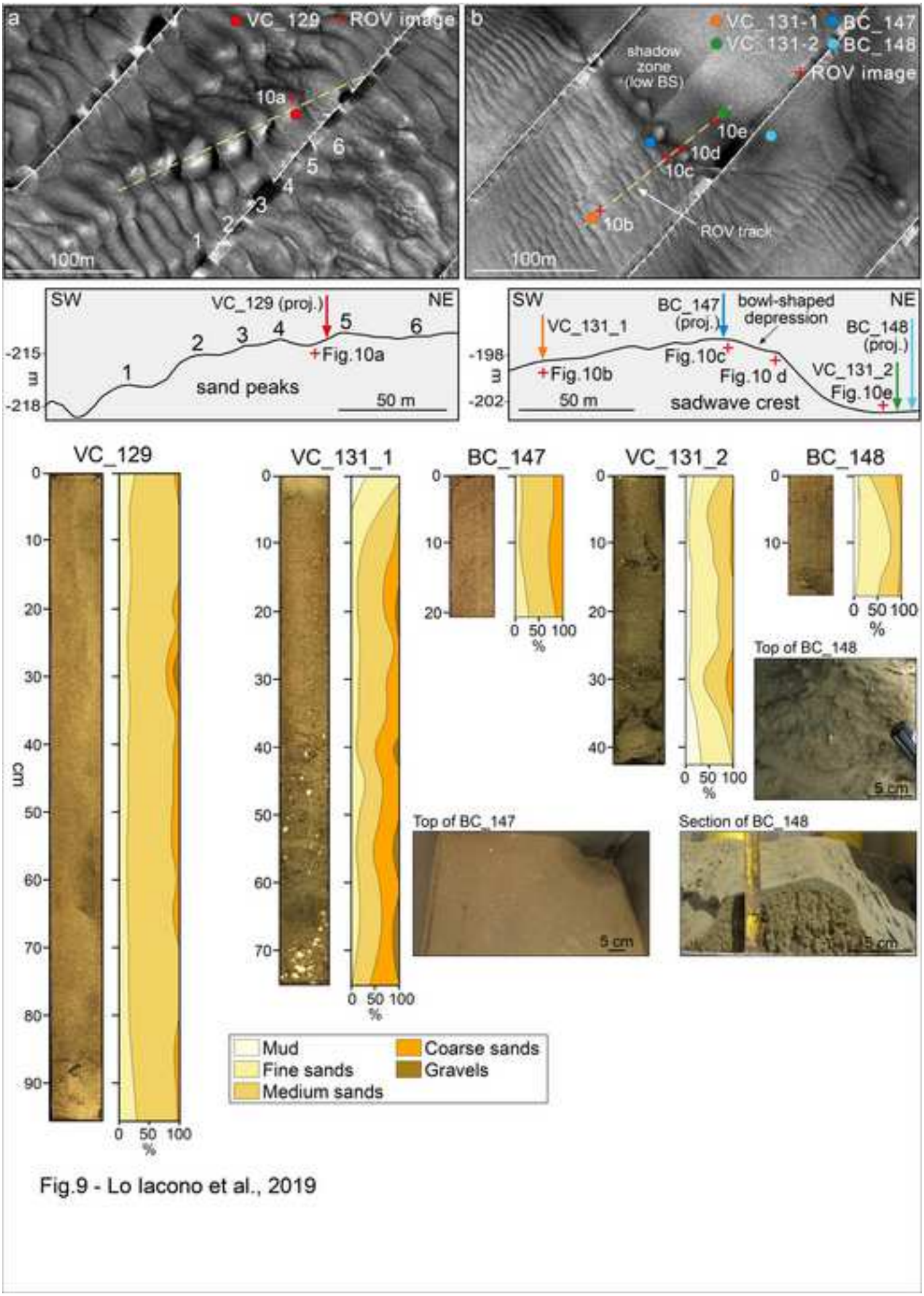

Fig.9 - Lo Iacono et al., 2019

Figure10_Lo Iacono et al., 2019

Click here to download high resolution image

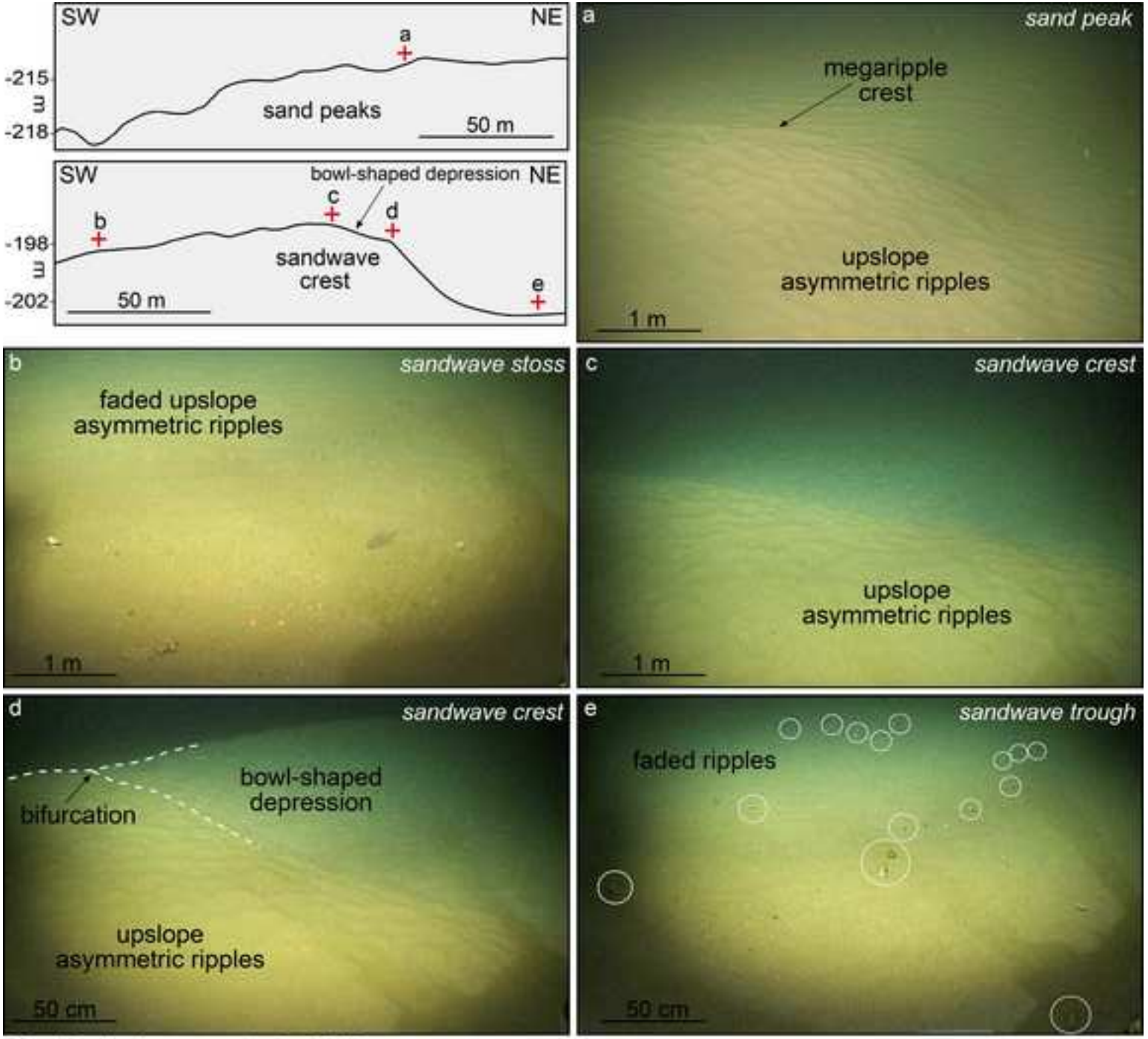

Fig.10 - Lo Iacono et al., 2019

Figure11_Lo Iacono et al., 2019
Click here to download high resolution image

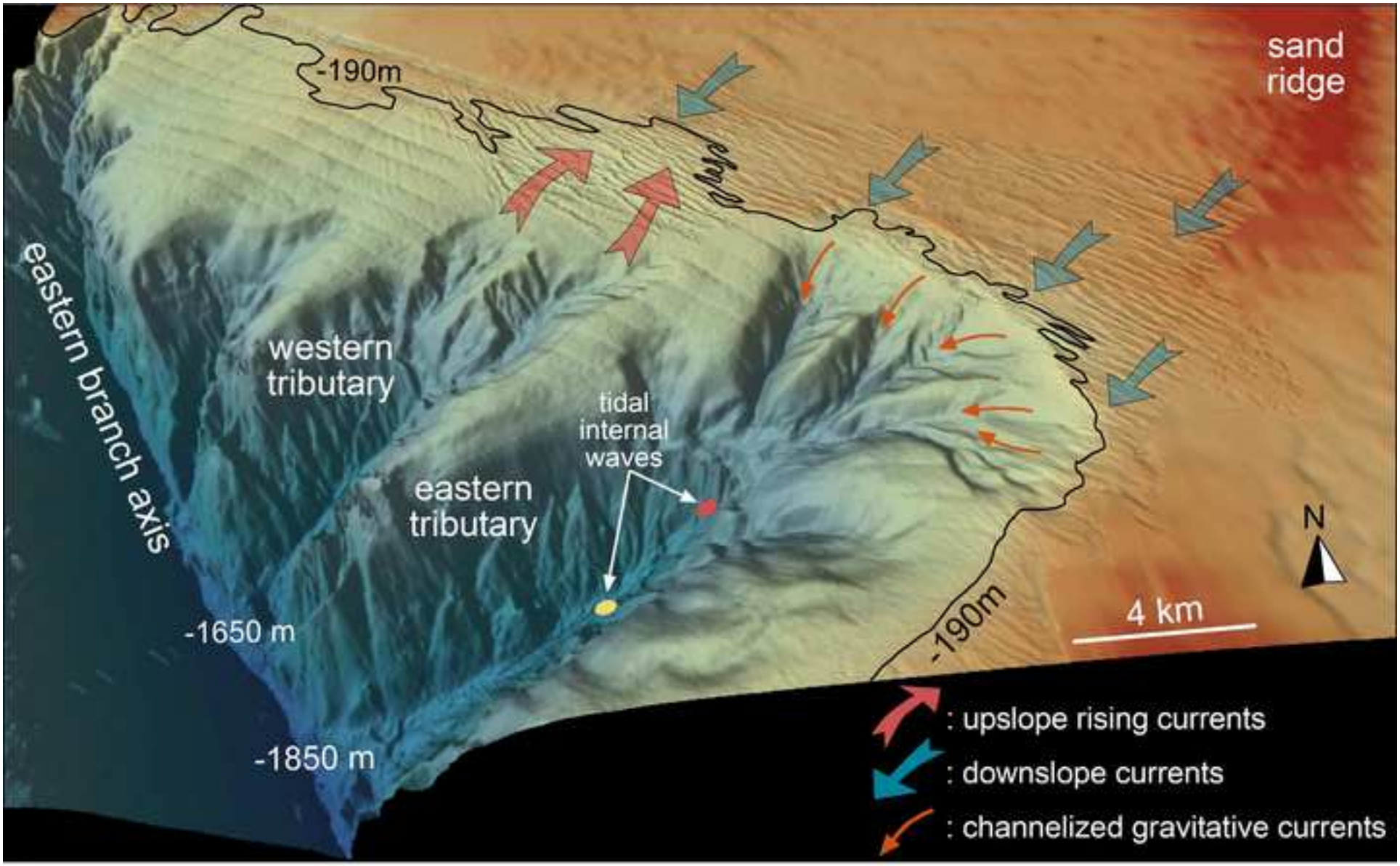

Fig.11 - Lo Iacono et al., 2019

Figure12_Lo Iacono et al., 2019
Click here to download high resolution image

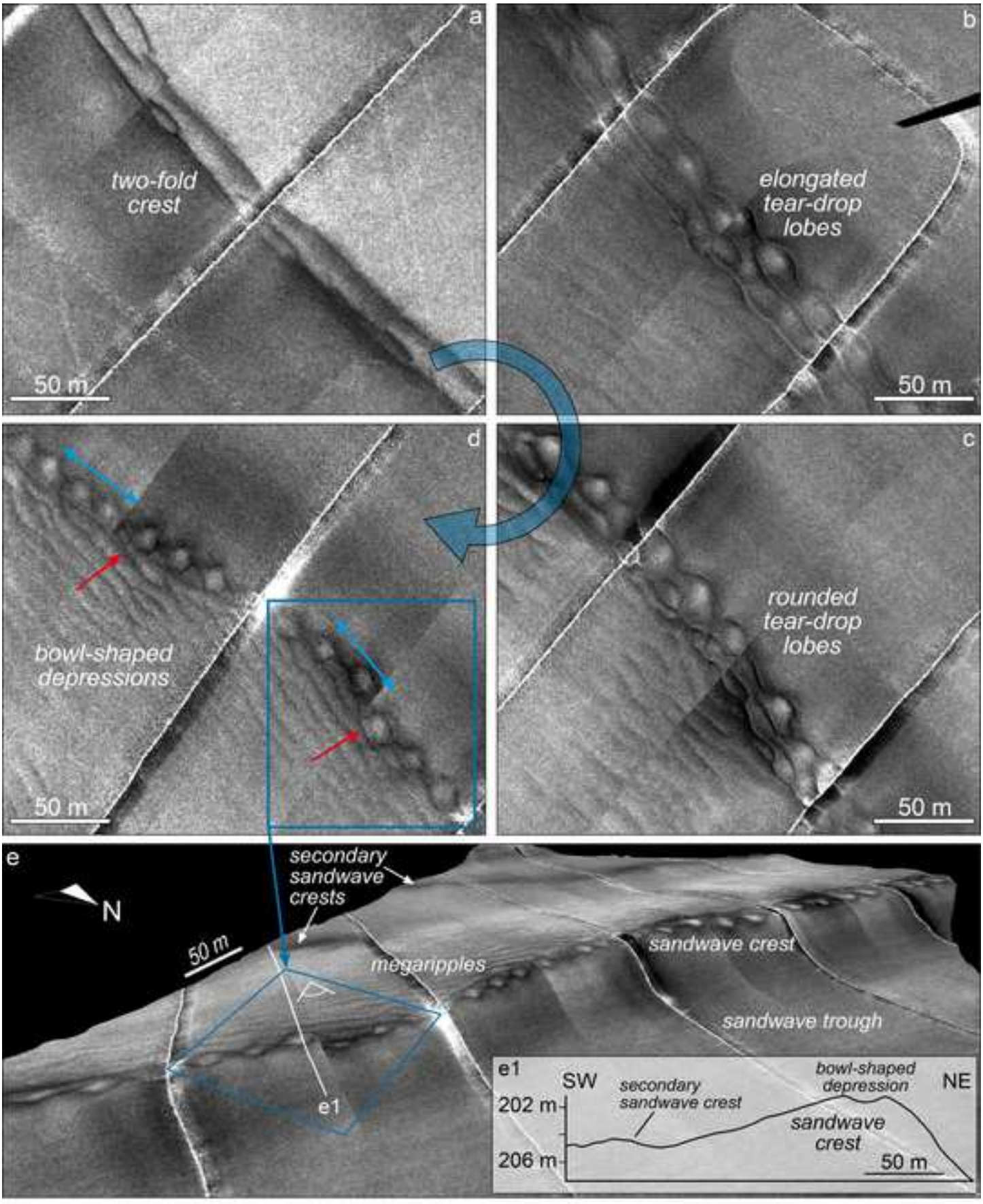

Fig.12 - Lo Iacono et al., 2019